

Master Thesis

**Evaluation, design and realisation of a
Riemann Pump for the frequency
range of 0..6 GHz for 5G mobile
communication**

Markus Weiß

Degree Programme: Embedded Systems Engineering

Matriculation Number: 3728492

Supervisor: Prof. Dr. Oliver Ambacher
PD Dr. techn. Rüdiger Quay

Period: 01.11.2015 – 02.05.2016

Freiburg, 02.05.2016

Declaration

I hereby declare that this thesis is my own work and effort and that all sources cited or quoted are indicated and acknowledged by means of a comprehensive list of references.

Freiburg, 02.05.2016

Markus Weiß

Abstract

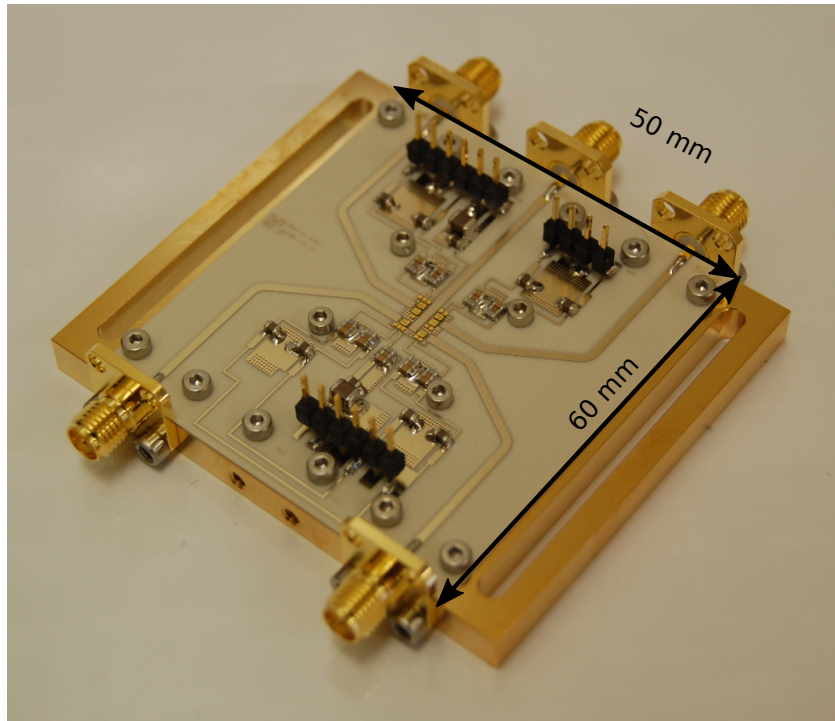


Fig. 0.1.: Built demonstrator

To the best of the author's knowledge, the worldwide first realised Riemann Pump in GaN technology is presented in Figure 0.1.

In this work a new concept of digital to analog conversion is investigated, yielding an arbitrary waveform generator which can be used in the next generation of mobile communication. This waveform generator is able to cover the frequency range from DC to 6 GHz, which simulations confirmed. With the help of this multi bit resolution of a charge pump, the actual conversion methods of digital to analog conversion are enhanced impressively.

The realised hybrid test circuit was designed, implemented and measured to proof the concept of a push-pull stage, functioning as a differential switch, providing a multi bit charge pump. The multi chip solution is chosen to proof the feasibility of the approach and to depict already trade offs which occur during the work.

Although the simulations confirmed the feasibility to cover the broadband frequency

range some practical drawbacks were mentioned, which limit the frequency range. As the generation of the signal wave form at the output of the circuit, generates much heat, two different concepts were demonstrated to deal with the heat spreading. As the energy consumption of modern digital to analog conversions with multi bit resolution is critical an approach is chosen which yields a good efficiency.

Zusammenfassung

In dieser Arbeit wird ein neues Konzept der Digital-Analog-Umwandlung untersucht, ein Arbitrary Waveform Generator ergibt, die in der nächsten Generation der Mobilkommunikation verwendet werden könnten. auf SI 6 giga Hertz, die bestätigt Simulationen: Diese Wellenform-Generator sollte den Frequenzbereich von gls dc ab abdecken können. Mit Hilfe dieser Multi-Bit-Auflösung einer Ladungspumpe, die tatsächlichen Umrechnungsmethoden Digital-Analog-Umwandlung kann verbessert werden.

Der realisierte Hybrid-Testschaltung wurde entwickelt, umgesetzt und bis zum Beweis das Konzept einer Push-Pull-Stufe gemessen, als Differenzschalter funktioniert, ein Multi-Bit-Ladungspumpe bereitstellt. Die Multi-Chip-Lösung wird die Machbarkeit des Ansatzes zu Beweis gewählt und bereits Kompromisse darstellen, die während der Arbeit auftreten. Obwohl die Simulationen bestätigt die Machbarkeit der Breitband-Frequenzbereich einige praktische Nachteile zu decken erwähnt wurden, die den Frequenzbereich zu begrenzen. Da die Erzeugung des Formsignals Welle am Ausgang der Schaltung, viel Wärme erzeugt, zwei unterschiedliche Konzepte wurden nachgewiesen mit der Wärmeverteilung zu behandeln. Da der Energieverbrauch der modernen Digital-Analog-Umwandlungen mit einer Auflösung Mehrbit ist entscheidend ein Ansatz gewählt, der einen guten Wirkungsgrad liefert.

Contents

List of abbreviations	iii
List of symbols	v
1. Introduction	1
2. Fundamentals of the Riemann Pump	3
2.1. Basic concept of software-defined radio for 5G mobile communication	3
2.2. System design using the Riemann Pump	5
2.3. Idea of the Riemann Pump	6
2.4. Riemann Code generation	9
2.5. Characteristics of Digital-to-Analog converter	12
2.6. Conclusion of the fundamentals	14
3. Riemann Pump circuit design	15
3.1. Approach and implementation of the Riemann Pump	15
3.2. Identification of the load impedance	17
3.3. Dimension of the used components	19
3.4. Identified problems	21
3.5. Circuit design summary	22
4. Circuit simulations for generating various waveform signals	25
4.1. Generating various analog signals with digital input control	25
4.1.1. Sine wave generation in the time domain	25
4.1.2. Full wave rectified sine wave generation in the time domain	31
4.1.3. Triangular wave generation in the time domain	32
4.2. Stability analysis of the realised circuit	34
4.3. Power consumption analysis of the realised circuit	34
4.4. Proof of concept simulation with existing components	36
4.5. Evaluation of the simulation results for the Riemann Pump	38
5. Realisation of a demonstrator	39
5.1. Substrate layout using DDRi_X6 and DDRi_Y6 chips	40
5.2. Substrate layout using DDRi_2C chips	43

5.3. Evaluation of the design and realisation process	44
6. Measurement of the realized circuit in the time domain	47
6.1. Measurement setup	47
6.2. Calibration and stability check	49
6.3. Time domain measurement of push-pull stage	50
6.4. Time domain measurement of synthesized signal	51
6.5. Discussion of measurement results	53
7. Conclusions and outlook	55
Bibliography	57
Appendix	64
A. Schematic of the Riemann Pump circuit for simulation	64
B. Schematic of the realized Riemann Pump circuit	66
C. Photography of the realized Demonstrator version 1	67
D. Photography of the realized Demonstrator version 2	68
E. SNR Calculation for simulated signals	69

List of abbreviations

ADS	Advanced Design System
Au	Aurum - Gold
AWG	arbitrary waveform generator
ChemNiPdAu	chemical Nickel Palladium Aurum
Cu	Copper
DAC	digital-to-analog converter
DC	direct current
DSP	digital signal processor
DUT	device under test
ESR	equivalent series resistance
FET	field-effect transistor
GaN	gallium nitride
HEMT	high electron mobility transistor
IAF	Fraunhofer-Institut für Angewandte Festkörperphysik
LNA	low noise amplifier
LTE	Long-Term Evolution
MAG	maximum available gain
MMIC	microwave monolithic integrated circuit
MSL	microstrip line
OSR	oversampling ratio
PCM	Pulse-code modulation
PLL	phase locked loop
RF	radio frequency
RF-FE	radio frequency front-end
SDR	software-defined radio
SMD	surface mounted device

SNR	signal-to-noise-ratio
SQNR	signal-to-quantization-noise-ratio

List of symbols

C_{out}	output capacitance
V_{dd}	positive supply voltage
V_{dn}	negative driver supply voltage
V_{dp}	positive driver supply voltage
V_{gs}	gate source voltage
V_{out}	output voltage
V_{ss}	negative supply voltage
$f_{Nyquist}$	Nyquist Frequency
$f_{sampling}$	sampling frequency/rate
$f_{signal,max}$	maximum signal frequency
f_{signal}	signal frequency
i_{out}	output current

1. Introduction

Description of the task.

Mobile communication became a major part of our daily life. With the release of the fourth mobile communication standard LTE (Long-Term Evolution), over seventy 70 power stations are in operation. In our every day life applications such as Instagramm, Whatsapp, facebook and Snapchat are dealing with very high data transfer rates. The industry also handles a very big amount of data. Real time trading at a stock exchange market is crucial, so the industry tries to reach this with the help of RF mobile communication. The data rate is increasing exponentially up to the year 2020. Todays hardware architectures can not handle this amount of data. In the next generation, the fifth, of mobile communication different concepts are needed to deal with this high data rate. In the next generation new hardware architecture are needed. This new concepts are based on the idea of a full software radio. The concept is basically to bring the digital domain as close as possible to the RF Front-End. Therefore the filter, mixer and computation would be much faster, more accurate and less complex.

In Chapter two some fundamentals are explain to get a better understanding of the work. Chapter three explains the design workflow to get to an working principle and a schematic. Chapter four evaluates the principle and after a successful simulation the layout is done in chapter five. after designing and layouting the schematic lastly the measurements are taken. in the end the results are discussed.

5G will be the gamechanger for autonomous driving. low latency (nearly realtime) and super high speed networks. Ten years ago the most shared thing was text, then it becomes pictures and nowadays it is video. But this is not the end of the line, the next step would be a 360 degree angle camera, 3 dimensional, high resolution live stream a la virtual reality. This would mean the next mobile communication standard, 5G, is an enhancement for high data rate and bandwidth and of course the low latency, near to real time transmission. Another topic will be the voice controlled everything, keyword IoT. The smartphone will be overcome with another gadget, most likely voice controlled. This voice control creates a lot more data than tipping it into the keyboard of a smartphone. 5G also means to connect the world, so Mark Zuckerberg. The next standard should be more efficient, cheaper and therefore it should be affordable for every country. Also it could be possible to cover those countries via satellite.

2. Fundamentals of the Riemann Pump

To place this work into the context of the next generation of mobile communication, a concept is described called software-defined radio. Implemented in this concept, the function, the benefit and some fundamentals of the Riemann Pump are described. A demonstrated system shows the SDR (software-defined radio) concept, which is based on the idea to bring the digital domain as close as possible to the antenna. The Riemann Pump is an arbitrary waveform generator which is controlled by a digital input signal, making it also a custom DAC (digital-to-analog converter). The concept of the custom designed DAC as well as some characteristics are presented. A concise discussion conclude the presented fundamentals.

2.1. Basic concept of software-defined radio for 5G mobile communication

The concept of software-defined radio is treated to overcome old problems of mobile communication and hence deal with a fast adapting system which can handle several mobile communication standards at once. New standards can handled since the system can be changed with an firmware update. Therefore every signal within the proposed bandwidth could be processed without changing the hardware, which made it software defined. The ability to process a spectrum of DC (direct current) to 6 GHz enables it to deal with future mobile communication standards.

To achieve this goal it is essential to bring the digital domain as close as possible to the antenna [1], [2],[3]. The digital domain has a lot of advantages regarding complexity, cost, filtering and processing speed [4], [5]. The structure of digital components is less complex and therefore has less cost. Digital filtering is more precise and data processing is more efficient and faster [6], [7].

The ultimate software defined radio architecture is shown in Figure 2.1.

In this vision the analog received signal is directly converted into the digital domain and afterwards filtered, mixed, demodulated and processed. For the transmission path the process is vice versa. The absence of the RF-FE (radio frequency front-end) is a dream still to come true [3].

Figure 2.2 shows the feasibility (left) and the estimated power consumption (right) eval-



Fig. 2.1.: Ultimate Software-defined radio architecture [2]

ated in [3]. The illustration shows that this vision is not a realistic option yet.

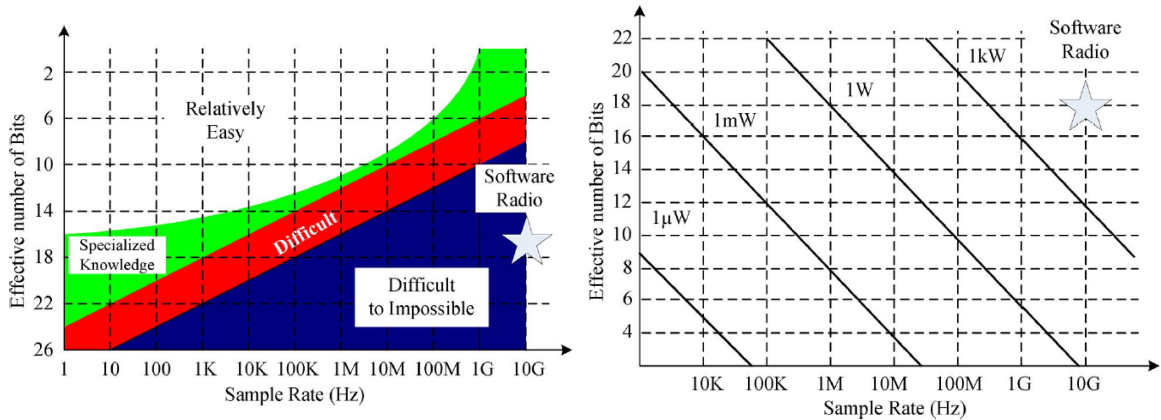


Fig. 2.2.: Feasibility (left) and estimation of energy consumption (right) regarding Effective number of Bits and Sample Rate [3]

To reach modern RF (radio frequency) standards a ENOB (effective number of bits) of 17 is required while ensuring a sample rate of 10 GHz to process baseband signals in the GHz range. As shown in Figure 2.2 on the left side, the development of an ADC (analog-to-digital converter) or DAC with modern technologies is difficult to impossible with respect of the mentioned requirements. Another critical bottleneck in this concept is the power consumption, shown on the right side. A power consumption in the range of kW occurs if the requirements for modern RF standards are fulfilled. This identification of drawbacks makes the analog RF-FE indispensable. The pre-processing of the analog signal in the receiving path is required to reduce the energy consumption to a moderate range. While for the transmitting path, the concept of the Riemann Pump comes into play.

2.2. System design using the Riemann Pump

The focus in this thesis was on the transmitting path of the mentioned system, since the receiving architecture and concepts need a separate investigation. Further details on the receiving concepts and investigations can be found in [1], [8], [9], [10]. Since the transmitting path is considered, the need for a DAC becomes visible, as the digital data must be converted to an analog signal before transmission. As mentioned before high demands are made to the DAC implemented in a SDR concept.

An important requirement is to keep the energy consumption in a moderate range. If the consumed energy is in the range of several kW (Figure 2.2) it is clear that this is unworkable. In order to meet RF standards the SNR (Signal-to-noise-ratio) has to fulfil the given limits. To achieve a moderate SNR, the resolution and the OSR (oversampling ratio) of the DAC have to meet the requirements. The generated analog output signal, which can consist of a few concurrent signals, has to be amplified for the propagation. To avoid unwanted distortions in the propagated signals linearity of the system is crucial.

Figure 2.3 demonstrates the transmitting path of the system design for the concept of SDR with the implementation of the Riemann Pump.

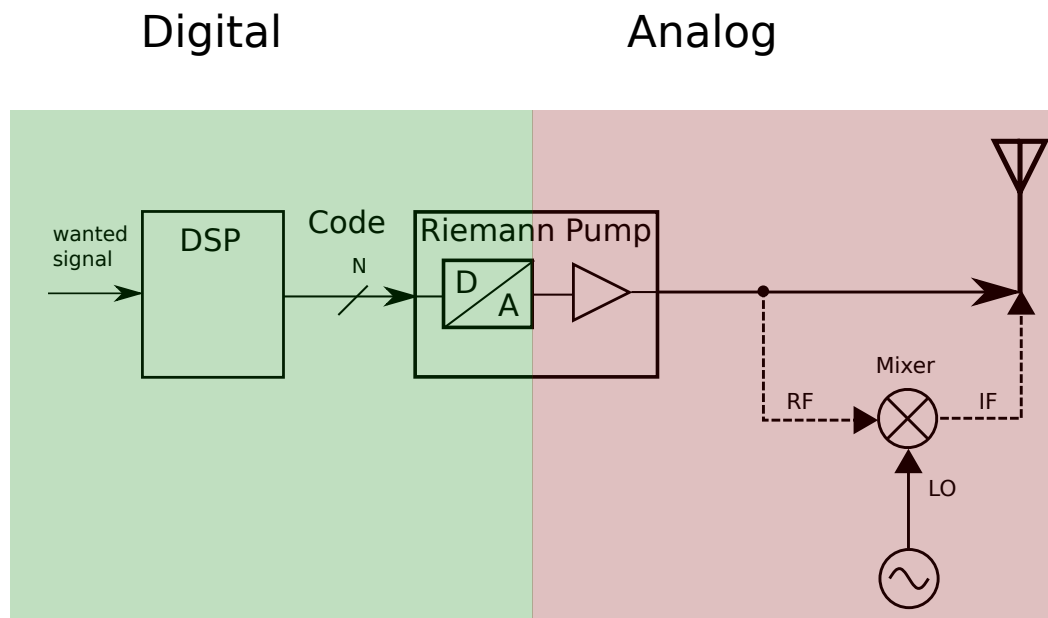


Fig. 2.3.: Concept of the Software-defined radio

The demonstrated path in Figure 2.3 is subdivided into a digital and analog part. The green digital part is responsible for the calculation of the desired signals and the generation of

the corresponding digital code. A theoretical wanted signal in the time domain, consisting of multiple modulated signals, is fed to a DSP (digital signal processor) which computes a digital bit-stream. The so called Riemann Code controls the input of a custom DAC, called Riemann Pump, which is the interface between the digital and the analog part.

In the red analog domain the desired signal is amplified by an implemented power transistor in the Riemann Pump and then propagated via the antenna. Optionally a mixer can be connected to mix the desired signal to even higher frequencies of several tenth of GHz.

Beside the advantages of the concept there are some constraints on the energy consumption as well as on the real time emission. Energy consumption is increasing linear with the switching frequency and therefore with the signal bandwidth. Secondly the real time emission is constrained due to the calculation and conversion of the Riemann Code.

2.3. Idea of the Riemann Pump

After the implementation in a system design has been demonstrated, the concept of Riemann Pump itself is explained.

The concept shown in Figure 2.4, is implemented in conventional PLLs (phase locked loops) and is known as a charge pump, which is the basic principle of the Riemann Pump [2], [11], [12]. Basically the inputs are switches and the output is a capacitance. The output capacitance (C_{out}) can take any value between the positive (V_{dd}) and negative (V_{ss}) power supply voltage by controlling the input switches.

The integration of the electrical current (i_{out}) at the capacitance (C_{out}), to form the output voltage (V_{out}), recalls the founder of the integration principle, Bernhard Riemann. This integration and the concept of the charge pump lead to the name Riemann Pump, first mentioned in 2013 [2].

Figure 2.4 shows the basic principle of a charge pump, used for the digital to analog conversion in this thesis.

Two switches are shown, which are capable to switch current to and from the output capacitance, respectively. The high side switch, which pushes charges onto the output capacitance, is connected to a current source at V_{dd} . In contrast to that, the low side switch is connected to a current source at V_{ss} . While controlling the switches with a differential input signal, the output voltage can be varied between V_{dd} and V_{ss} . As the control signal only consists of closing and opening a switch, a digital signal is sufficient. If the high side switch is closed while the low side switch is opened, charges are pumped to the capacitance which leads to an increase in output voltage. This effect only takes place if the control signal is differential, which leads to synchronous switching behaviour of both switches.

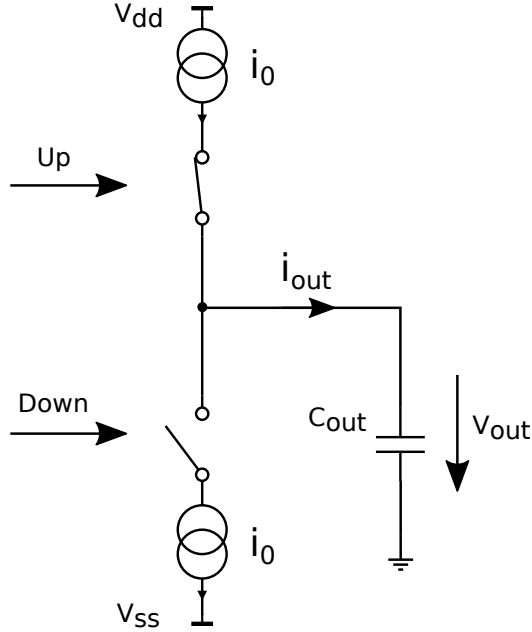


Fig. 2.4.: scheme of a charge pump

Otherwise the controlling of the output voltage is not defined. If both switches are closed at the same time, the potential at the capacitor is floating and hence no defined voltage can be stated. For decreasing the output voltage the low side switch has to be closed, while the high side switch is open, to allow the capacitor to discharge.

Corresponding to the described principle, the output voltage

$$V_{out} = \frac{1}{C_{out}} \int_0^T i_{out}(t) dt \quad (2.1)$$

is calculated by integrating the current over time.

A custom DAC is created by extending the basic charge pump with several other charge pumps in parallel, as seen in Figure 2.5. Since the output voltage, consisting of the desired signals, should be propagated via an antenna, the output capacitance C_{out} can be interpreted as the input stage of a linear power amplifier. This input stage consists of a power transistor, which do have the capacitive input impedance characteristic. Implemented in one component this concept saves area and costs and the amplified signal at the drain can be transmitted via the antenna.



Fig. 2.5.: Concept of the Riemann Pump with three-bit resolution

The dimensions of the current sources, connected in parallel, have to increase by the power of two to get a defined set of currents. Otherwise two states would share the same code which will lead to a loss of information. Demonstrated is a DAC with three bit resolution, which leads to eight different output currents. Instead of using absolute current values, relative currents with respect to i_0 are used.

2.4. Riemann Code generation

The three bit resolution leads to eight different slopes which are presented in Figure 2.6.

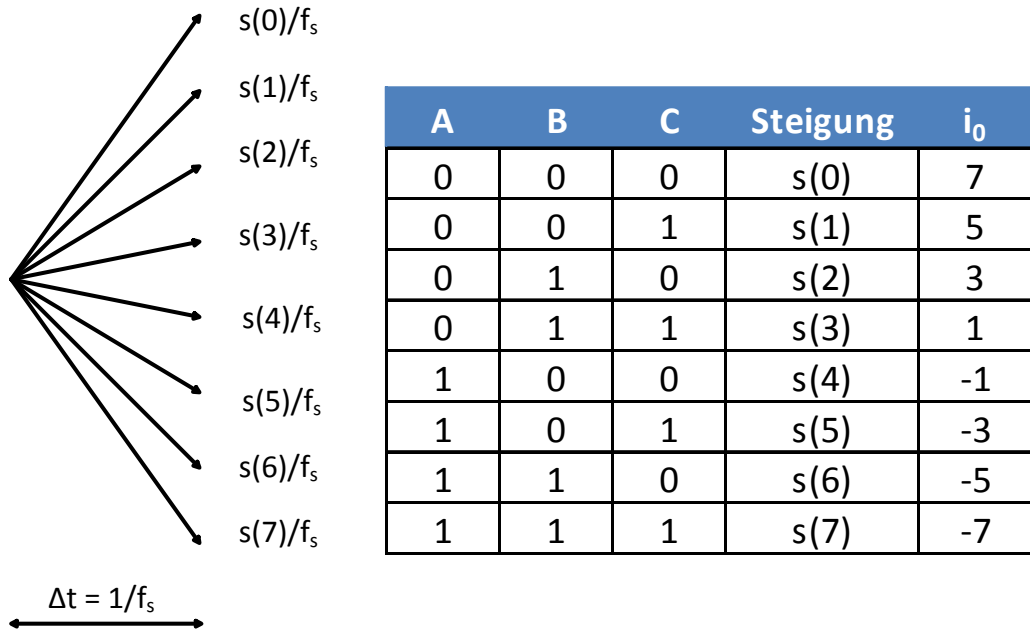


Fig. 2.6.: slopes and corresponding code of the synthesized signal

Corresponding to the demonstrated eight different slopes on the left side, a table is presented which states the corresponding encryption for each slope on the right side. For example the representation of the relative slope of $-1i_0$ is: $100 \equiv s(4)$. Each digit of the code states the position of the corresponding switches (A, B and C), that is 0 for opened and 1 for a closed switch. Figure 2.7 shows the principle of the generation process.



Fig. 2.7.: Code generation principle

This principle states that a sampled version of the desired signal exists (y_s) which is subtracted by a linear approximated signal y_r to obtain the error which then is minimized. For every sampling point k , the relative slope $s(m)$ (m belonging to $[0, 2^N - 1]$; N number of bits) is chosen which minimizes the quantization error

$$e(k) = |y_s(k) - y_r(k)|. \quad (2.2)$$

The estimated value of $y_r(k)$ is represented by the sum of its previous value and the chosen slope times the sampling interval ($\frac{1}{f_{sampling}}$) yielding:

$$y_r(k) = y_r(k - 1) + \frac{s(m)}{f_{sampling}}. \quad (2.3)$$

An advantage of this concept is that the quantization is done with the range of the maximum deviation of the slopes, since always two successive samples are taken. Therefore the quantization does not need the whole dynamic of the signal. The estimated signal y_r (Equation 2.3) thus presents the sampled signal and generates the corresponding Riemann Code. The benefit of the closed loop principle is that the recovered signal after integration, does not drift. In comparison to this, in an open loop principle the difference between the current $y_s(k)$ and the previous input sample $y_s(k - 1)$ is quantified and thus lead to a cumulative error in the recovered signal [13]. An illustration of the closed loop generation of the Riemann Code is shown in Figure 2.8.

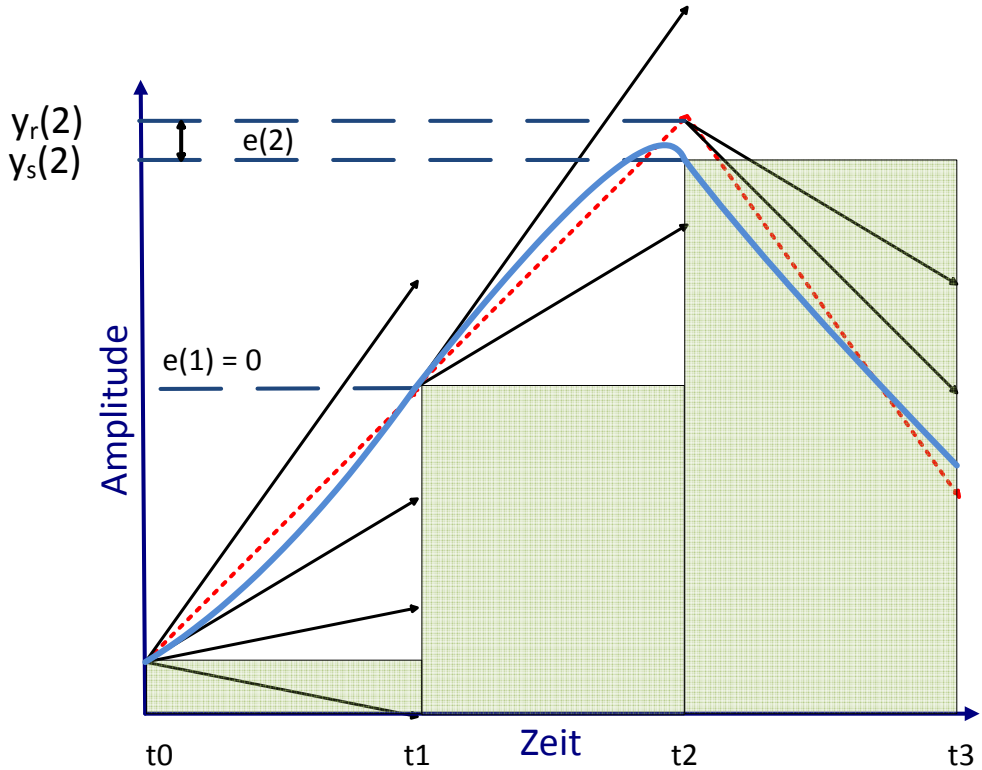


Fig. 2.8.: Code generation - error minimizing

The blue signal is the desired sampled input signal, the red is the linear approximation of the signal which generates the Riemann Code. For the sampling point at time t_1 no error exists since the linear approximation fit perfectly to the sampled input signal. At the discrete time point t_2 the slope $s(m)$ was chosen which minimized the error stated in Equation 2.2. The chosen slope is encrypted with the digital representation as shown in Figure 2.6. This principle is used in an iterative way to generate a full sequence of slopes for the desired signal. This sequence of slopes represents the Riemann Code for the desired signal. Figure 2.9 illustrates an example for generating a Riemann Code.

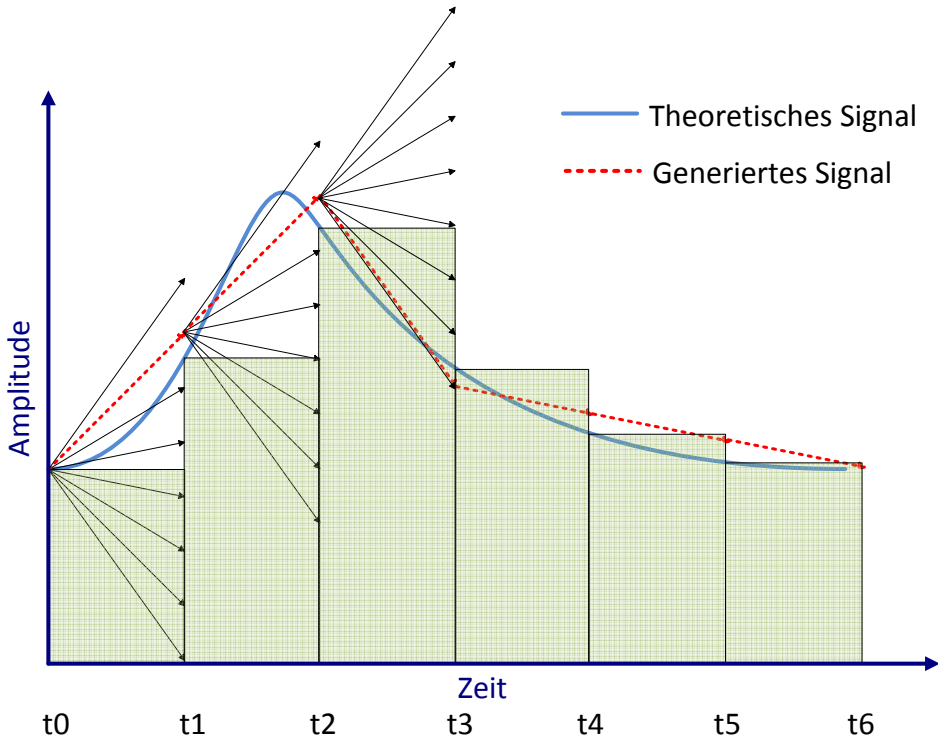


Fig. 2.9.: Integral of the current which pumps charges on to the cap.

In this example the sequence of slopes is

$$s(1) \ s(1) \ s(7) \ s(4) \equiv +5i_0 \ +5i_0 \ -7i_0 \ -1i_0, \quad (2.4)$$

for the time interval $[t0, t4]$ which generates the Riemann Code:

$$001 \ 001 \ 111 \ 100 \ . \quad (2.5)$$

The desired signal, consisting of multiple different signals where each can have a different modulation and symbol rate, is pre processed and then sampled with the Riemann Conversion. Using this technique arbitrary waveforms can be generated avoiding that the signal drift.

2.5. Characteristics of Digital-to-Analog converter

To reach modern RF standards, a minimum amount of resolution and oversampling is needed. Oversampling is crucial for the recovery of a signal, due to the Nyquist-Shannon sampling theorem

$$f_{Nyquist} = 2f_{signal,max}. \quad (2.6)$$

This Nyquist Frequency is the minimum sampling frequency for the correct recovery of a signal. That means the actual sampling rate $f_{sampling}$ (sampling frequency) has to be at least two times $f_{signal,max}$ (maximum signal frequency).

Every increase of $f_{sampling}$ above the $f_{Nyquist}$ (Nyquist Frequency) is called oversampling. To increase the performance of the DAC an OSR is introduced [12]:

$$OSR = \frac{f_{sampling}}{2f_{signal,max}}. \quad (2.7)$$

As the SNR is presented in the context of the digital-to-analog conversion, it is equivalent to the SQNR (Signal-to-quantization-noise-ratio) as both is based on the quantization error. Tuning the two parameters, resolution and OSR, results in an increase of the SNR, as illustrated in 2.10 [12].

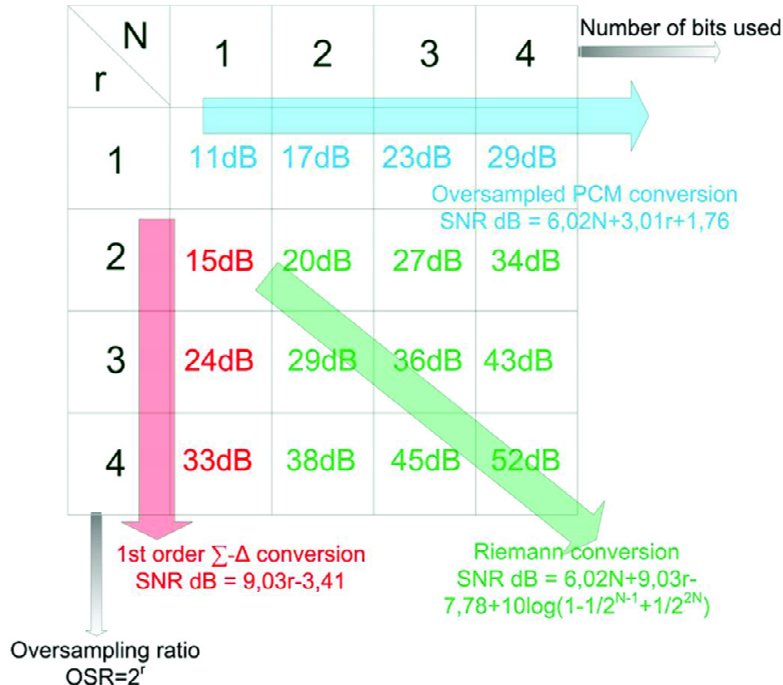


Fig. 2.10.: Table of theoretically SQNR for a full scale sine wave over resolution and OSR [12]

The table states the theoretical achievable SNR with respect to these two parameters. The parameter N describes the number of bits used for the resolution and r the binary logarithm of the OSR, respectively. Here the OSR is defined as

$$OSR = \frac{f_{sampling}}{2f_{signal,max}} = 2^r, \quad (2.8)$$

which leads to

$$f_{sampling} = 2^{r+1} * f_{signal,max} \quad (2.9)$$

with respect to r . As you can see in Figure 2.10 the Riemann Conversion (green) performance is the best for a minimum number of bits and a OSR, with respect to the parameter r , of two. Performing a digital-to-analog conversion with one bit resolution, the $\Sigma - \Delta$ conversion fits the best. For $r = 1$ the PCM (Pulse-code modulation) conversion yields the best SQNR.

In the Riemann Conversion it yields, that every increase in the number of bits will increase the SQNR by 7 dB, while increasing the parameter r , will increase the SQNR by 9 dB [13].
Equation 2.10

$$\text{SNR [dB]} \approx 6.02N + 9.03r - 7.78 + 10 \log_{10}\left(1 - \frac{1^{N-1}}{2} + \frac{1^{2N}}{2}\right) \quad (2.10)$$

stated an approximation to calculate the theoretical achievable SNR for a full scale sine wave with the Riemann Conversion [12]. For the sake of simplicity the formula 2.10 was not derived in this context. For further details see [11],[13] and [14].

2.6. Conclusion of the fundamentals

In contrast to classical current steering topologies the Riemann Pump concept rather makes use of the derivative at sampling points than to sample the absolute value. In order to reconstruct the analog signal, the digital code thus has to be integrated.

In this chapter the implementation of the Riemann Pump in a system design has been presented. After the description of the classification and application, the concept of the custom DAC has been described. After explaining a simple charge pump, a multi bit resolution DAC have been presented. The designed custom DAC has been compared to conventional DAC concepts. A concise evaluation states that the Riemann Pump is a great improvement for conventional digital-to-analog conversion concepts.

3. Riemann Pump circuit design

The goal was to design an arbitrary waveform generator for a signal bandwidth of 6 GHz. For the implementation in a base station, the most promising technology was GaN (gallium nitride). GaN HEMTs (high electron mobility transistors) were used for the high speed switches, which served as voltage controlled current sources. Based on the chosen technology a suitable push-pull concept were found [15] to show the feasibility of the concept. The attention was rather drawn to proof the concept than to optimize for energy consumption or efficiency. In the design process a suitable load impedance and the right dimension of the used components had to be found.

3.1. Approach and implementation of the Riemann Pump

As stated in chapter 2.3 the circuit needed high speed switches, which were capable to drive power. In order to switch a HEMT transistor to the high side power rail a driver circuit was needed, since in GaN no complementary transistors were available. The absence of a p-type transistor in GaN technology made it challenging to find a suitable concept to realize the push-pull stage. The n-type HEMTs operating in depletion mode needed a negative gate source voltage V_{gs} (gate source voltage) to switch the transistor off. For the on switching V_{gs} had to be 0 V and therefore a driver circuit was needed, since the source potential of the high side switch varies between V_{dd} and V_{ss} . The source contact of the high side switch, realized by a n-type GaN HEMT, was connected to the output of the test circuit and therefore the potential at the output was not constant. A suitable driver circuit was found in [15], where the principle of a push-pull stage for power applications is described.

One possible approach to design a Riemann Pump is shown in Fig. 3.1.

On the left side, as marked, is the driver circuit which was needed to switch the high side transistor without dissipating a huge amount of power. As the timing is crucial for the switching process, the driver concept was implemented for the low side switch too. Each driver consisted of a base transistor, marked as $Qb1$ and $Qb2$, which served to operate as a inverter. Also two load transistors, $Ql1$ and $Ql2$, were implemented with a source degeneration resistor which served as a current source. The resistors $R1$ and $R2$ were

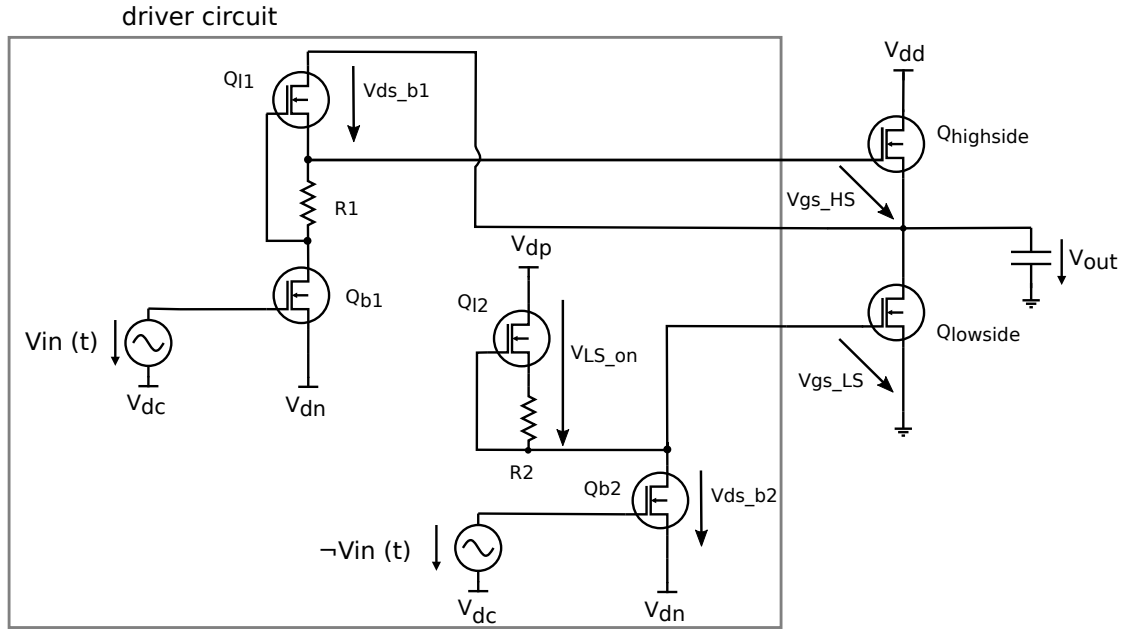


Fig. 3.1.: Schematic of a push-pull stage with corresponding driver circuit

tuned to provide a proper current while maintaining a decent power consumption. If the resistors were set to a low value, the current source provides more current and hence the switching process is faster since the charging of the gate capacitance of the high and low side transistors is faster. But a draw back was that for the higher current a higher power consumption occurred. In addition to the driver circuit two power transistors were implemented which demonstrated the one bit DAC. These two transistors, $Q_{highside}$ and $Q_{lowside}$, represented two switches which switch the output to the high side power rail and low side power rail, respectively. Switching the high side transistor ($Q_{highside}$) to the on state required a gate-source voltage V_{gs_HS} of 0 V. This is achieved by the feedback path from the output to the drain of the load transistor (Q_{l1}) which also turns on and in fact of the low on resistance the voltage drop of $V_{ds_b1} \approx 0V$ ($\equiv V_{gs_HS}$). The transistor Q_{l1} is turned on because $V_{gs_b1} = 0V$ since the base transistor Q_{b1} is turned off and hence no current is flowing. Switching from the on to the off state occurred when the base transistor Q_{b1} is switched on with a control voltage. When the base transistor is turned on, the gate potential of the high side transistor is set to approximately V_{dn} , by discharging the gate capacitance with Q_{l1} and $R1$ which served as a current source. The dimension of Q_{l1} and $R1$ determined the discharge current for $Q_{highside}$ and hence the switching speed and the power losses. Because $Q_{highside}$ is turned on if Q_{b1} is turned off and inversely, this act as a inverter structure. In addition to the presented principle of the high side switch the low side circuit operated in the same way but inversely. When the high side switch is turned on, the low side is turned off and vice versa. The benefit of the integrated driver circuit was the improved efficiency of switching. The transistor switching speed was determined

by the dimension of the driver circuit. The schematic shows the first approach for realizing a Riemann Pump in GaN technology. The next step was the identification and calculation of a proper output capacitance, since it represented the input of a linear power amplifier where the desired signal is synthesized.

3.2. Identification of the load impedance

Due to the fact that the signal is generated at the input stage of a linear power amplifier, as described in chapter 2, it was crucial to obtain its input impedance. The input impedance of the power amplifier was at the same moment the output impedance for the test circuit. This output stage of the test circuit is modelled with a GaN HEMT with a gate length of $0.25\text{ }\mu\text{m}$. Considering a 20 W power amplifier for transmission purposes, led to a GaN HEMT with a total gate periphery of 4 mm, based on an approximation for the power density of $5\frac{\text{W}}{\text{mm}}$ gate periphery [5], [16]. Simulations confirmed this approximation as an output power density of $5.6\frac{\text{W}}{\text{mm}}$ at $V_{GS} = -1.5V$, $V_{DS} = 25V$ was measured. The transistor model used in ADS (Advanced Design System) were modelled at the IAF[17] and is based on a state-space approach. For simulation purposes four transistors were modelled in parallel, each with 8 finger and $125\text{ }\mu\text{m}$ gate width to reach the required gate periphery. The simulated power amplifier is biased with respect to the maximum MAG (maximum available gain), which led to a bias of $V_{GS} = -1.5V$ at $V_{DS} = 25V$. After the determination of the bias point, a S-parameter simulation yielded the input reactance of the power amplifier. It is to note that the short analysis of the impedance was done with four power transistors in parallel representative for a power amplifier than a discrete model of a broadband amplifier. But since it was not the main goal to obtain a proper input impedance of a broadband amplifier this identification was sufficient. Hence this was a short and effective way to obtain an output impedance according to the equivalent circuit of a HEMT device as shown in Figure 3.2.



Fig. 3.2.: RF equivalent circuit FET [18]

The input of the HEMT is determined by the capacitances C_{gs} and C_{gd} , since the inductance is effective only for high frequencies. This capacitive behaviour is seen in Figure 3.2 for the gate node, which served as the input. As only the capacitive behaviour of the load impedance was of interest, the real part was neglected. The complex impedance is defined as

$$Z = R + jX, \quad (3.1)$$

where R is the real part and X is the electrical reactance. The electrical reactance X is defined as:

$$X = X_L + X_C = \omega L - \frac{1}{\omega C}, \quad (3.2)$$

and is plotted for the input of the test power amplifier in Figure 3.3 over the frequency range from nearly DC to 6 GHz in a logarithmic scale.

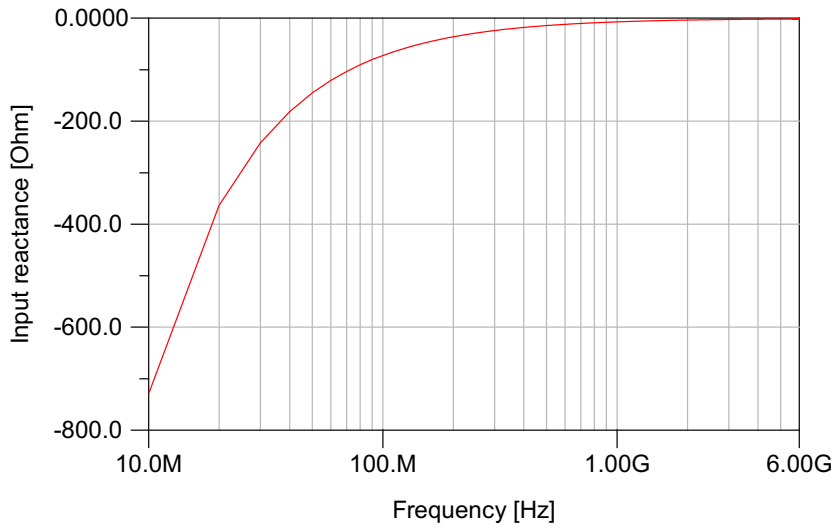


Fig. 3.3.: Load reactance over frequency in logarithmic scale

The constant increase of the reactance to nearly 0Ω confirmed Equation 3.2, since the main part of the reactance is determined by X_C . The capacitive reactance X_C is defined as:

$$X_C = -\frac{1}{\omega C}, \quad (3.3)$$

and thus the reactance scales with the reciprocal value of ω . The input capacitance C_{in} determined by the sum $C_{gs} + C_{gd}$, was calculated and yielded $C_{in} \approx 20\text{pF}$. Consequently this capacitance is used for further investigation as a load impedance.

3.3. Dimension of the used components

An input capacitance of nearly 20pF was found for the output linear power amplifier stage. Based on this calculation a proper test circuit was investigated. To avoid immediate clipping of the signal at the output, the transistor dimension had to fit, since an oversized transistor would fully charge the capacitance and the signal would be clipped. Hence a transistor dimension was chosen which allowed to synthesize a decent signal. To synthesize a sine wave for the frequency of 6GHz with a voltage swing of $V_{swing} = 4\text{V}$, the two greatest slopes were chosen. In the presented concept the resolution is three bit, hence eight different current slopes could be generated. The sequence of the relative slopes $7i_0$ and $5i_0$ synthesizes the rising edge of the sine wave. With this relative slopes and an oversampling ratio of four at the frequency of 6GHz , led to a sampling time Δt of 20.83ps , since the sampling frequency is eight times the signal bandwidth.

The current-voltage relation for the capacitor

$$I = C \frac{dU}{dt}, \quad (3.4)$$

is used to determine the reference current i_0 .

A voltage swing of $V_{swing} = 4V$ is equal to an amplitude of $\hat{v} = 2V$. The oversampling of four yielded, that the sine signal is sampled by eight points. Hence the rising edge consisted of two sampling points. The first sampling point with the relative slope of 7 and the second of 5, respectively. Integrating the current for two different samples yield:

$$\int_{\Delta t} 7i_0 d\tau + \int_{\Delta t} 5i_0 d\tau = C * U, \quad (3.5)$$

and solving for i_0 resulted in:

$$i_0 = \frac{U * C}{12 * \Delta t}. \quad (3.6)$$

For the assumption to reach nearly a voltage of $U = 2V$ for two sampling intervals ($2\Delta t$) and the capacitance of 20 pF it resulted a reference current of $i_0 = 160$ mA. As simulations showed, a reference current of 151 mA could be established with a dimension of the voltage controlled current source, high side switch, of $UGW = 100$ μm and gate finger number of eight. Hence the gate periphery for the reference current source is 800 μm . To ensure proper switching the driver circuit dimension had to be optimized. Since the driver circuit worked as a current source, the dimension of the transistors and resistors were tuned to achieve a proper current to switch the power transistors fast and efficient. The dimension of the driver transistors were approximately a quarter of the power transistors, the switching high and low side transistor. The resistor values were achieved by tuning with respect to power consumption. Further details on the driver circuit and its properties are stated in [15]. Figure 3.4 demonstrates one bit of the realized circuit.



Fig. 3.4.: One bit of the realized circuit

The schematic is designed with ADS and the full circuit design can be seen in Appendix A. For the full schematic it is to note that the dimension of the power transistors scales with the factor of two and so the driver circuit dimension do.

3.4. Identified problems

During the design process some problems already occurred. The major problem was that the current sources could not be defined as necessary. One requirement to use a GaN HEMT as a voltage controlled current source is depicted in Figure 3.5. In this simulation an unloaded transistor with eight gate fingers and a gate unity width of 125 μm was used. Figure 3.5 shows the output characteristic of a GaN HEMT in depletion mode for V_{gs} of 0 V (red) and -5 V (black). The blue line marks the transition from the linear to the saturation region. The on state is marked red with a gate-source voltage of 0 V. If the transistor is switched off no current is flowing, refer to the black curve with gate-source voltage of -5 V. To ensure that the GaN HEMT in depletion mode acts as a voltage controlled current source, it is necessary that $V_{gs} = 0V$ and $V_{ds} \geq V_{ds,sat}$. Hence the transistor had to be in the saturation region. The simulation yielded a drain-source saturation voltage of approximately 3 V. For the linear region, $V_{ds} < V_{ds,sat}$, the transistor acts as a resistor than a defined current source. This condition made it difficult to generate a reference current. Therefore a requirement would be, that the output voltage only vary between $V_{ss} + V_{ds,sat}$

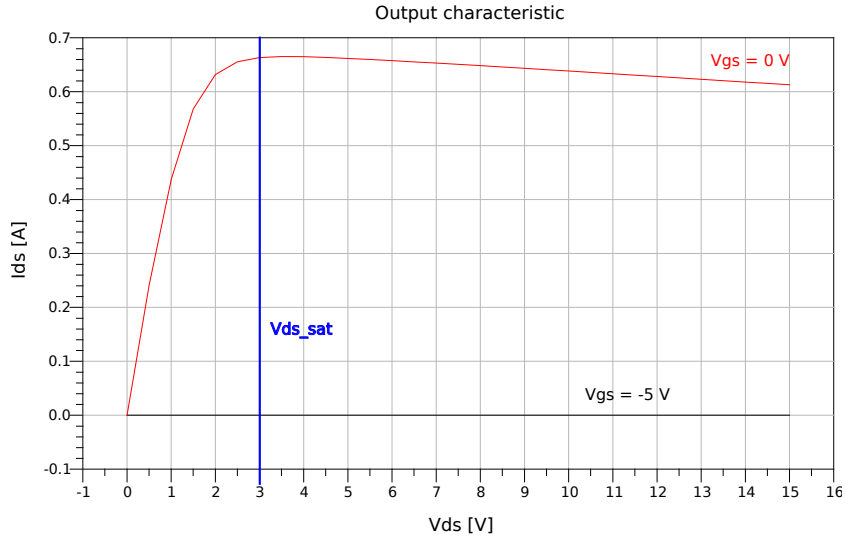


Fig. 3.5.: Output characteristic of a GaN HEMT in depletion mode

and $V_{dd} - V_{ds,sat}$. Once this limit is reached the current is not defined any more. As simulation showed, this problem occurred for both the high and the low side switching transistor and can be seen that the relative slopes do not scale with the presented slopes. In addition to this non ideal switching occurs which made it necessary to average the current over time. The problem of not perfect switching is, that the channel is opened and closed slowly in comparison to an ideal switch and hence the current do not switch from zero to i_0 rather slowly increase. A leakage current over the driver circuit is observed which further increase the problem. It is to mention that every push-pull stage had to handle this problem and therefore the relative slopes are considered, but the stages differed in the behaviour of switching and hence $3i_0$ is not perfectly $3 * 1i_0$. The different behaviour for the switching process of the separate push-pull stages led to a not precisely set of slopes. Reason for this was the leakage current of the driver network for the discharging process of each bit.

3.5. Circuit design summary

As no complementary transistors were available in III-V technology, a proper driver circuit had to be investigated. Further the speed of the switches was crucial as a broadband signal should be synthesized, which led to the implementation of a known concept [15] for the driver circuit. A low loss, high speed, digital controlled driver circuit was implemented which had the advantage to be verified and validated. The circuit design and simulation combines the DC state with the RF state, since for a DC simulation the current through a capacitor is zero. The dimension of the used components with the sampling interval determined the resulting voltage step. A draw-back was that a small transistor dimension could synthesize signals to a very low signal frequency while a bigger one would fully

charge the output capacitor which will clip the output signal. If the transistor dimension is chosen to be bigger, the higher signal frequency could be synthesized with a decent voltage swing but the low signal frequencies would turn into a rectangular shape. Therefore the dimension of the used components already limit the bandwidth. The signal bandwidth was investigated to be smaller than DC to 6 GHz. The used components were tuned with respect to the signal integrity over the frequency range of nearly 1.5 GHz to 6 GHz.

4. Circuit simulations for generating various waveform signals

Circuit simulations were run to validate the behaviour of the conceptual design and to present the trade offs. A harmonic balance simulation was used to investigate the concepts of chapter 3, as it presented a steady state solution neglecting the transient state. This frequency domain simulation was run with the tool ADS to present the solution for the nonlinear behaviour of the test circuit. In a first step the generation of various analog output signals were investigated. Three basic signal waveforms were synthesized to show the ability of generating different signals. Afterwards the designed test circuit of chapter 3 was tested with respect to stability and its energy consumption. As the realized circuit differed a bit from the presented test circuit in chapter 3, another simulation was run to get an impression what to expect for the measurement. The presented simulations were run with the schematic shown in appendix A, except for the simulation of the built demonstrator in chapter 4.4.

4.1. Generating various analog signals with digital input control

Generating analog signals from a digital input signal was the aim of the presented work. The designed custom DAC, the Riemann Pump, should be able to synthesize various waveform signals at the output. Simulation results were presented in the time domain to validate the integrity of the desired signal. In the system design a pre processor is used to compute the Riemann Code with a specific algorithm. For simulation purposes the digital Riemann Code was computed manually, as seen for example in Figure 4.1. A prerequisite for the design process was a resolution of the DAC of three bits. Another prerequisite was an OSR of four, as discussed in chapter 2. The presented simulations of the digital-to-analog conversion were run to proof the concept of the designed test circuit.

4.1.1. Sine wave generation in the time domain

As known from basic signal processing, the sine wave for continuous time is the elementary signal and therefore synthesized first. For the generation of this sine wave a corresponding

Riemann Code was required which will be converted to the desired sine wave.

This Riemann Code was generated by hand via an approximation of a sine wave with a sequence of eight different slopes. Eight different slopes represented the three bit resolution while the sequence of eight sampling points represented the OSR of four. Figure 4.1 illustrates this approximation to get the corresponding Riemann Code.



Fig. 4.1.: One possible approximation of a sine wave generation to get the Riemann Code

The sequence of chosen slopes, referred to i_0 values, is:

$$+7 \quad +3 \quad -3 \quad -7 \quad -7 \quad -3 \quad +3 \quad +7, \quad (4.1)$$

which represents the following encryption:

$$000 \quad 010 \quad 101 \quad 111 \quad 111 \quad 101 \quad 010 \quad 000, \quad (4.2)$$

based on the encryption table in Figure 2.6, chapter 2. The generated Riemann Code consists of eight triplets, where each triplet represents the three bit resolution. The quantity of digits in each set, here triplet, increases with the number of bits used for the resolution. The number of triplets represents the number of sampling points, corresponding to the OSR. This particular generated Riemann Code in equation 4.2 was used to synthesize sine waves in the frequency range between 500 MHz and 6 GHz, as shown in Figure 4.2.

The amplitude of seven signals with different frequencies are shown over their period while at the top the number of sampling points is shown. This representation is chosen to compare the signal integrity of different frequencies. The shape from most of the plotted functions fit fairly to a theoretical sine wave. As the sampling interval differs for different frequencies, the amplitudes of the signals also differed. The maximum reachable amplitude was the positive supply voltage, here set to 15 V, while the lower bound was

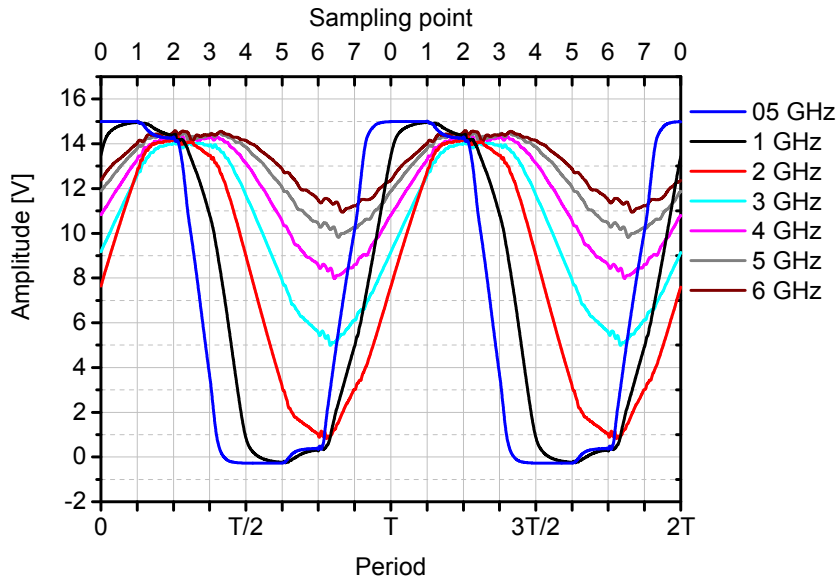


Fig. 4.2.: Synthesized signals with demonstrated Riemann Code for the frequency range of 0.5 GHz to 6 GHz

0 V. Once the amplitude reached the supply voltage, the signal wave form is clipped due to a fully charged output capacitor. This undesired effect transformed the sine wave into a rectangular shaped signal form, as seen for the blue and black curve. Therefore a bandwidth limitation is introduced.

Figure 4.2 highlights a limitation of the designed circuit as the blue curve turns into a rectangular signal form.

Below the frequency of 1 GHz the desired shape of a sine wave was transformed to a rectangular form due to the long sampling time. In addition to the unwanted rectangular form another distortion occurred, depicted in the blue signal for the sampling interval 1 to 2 and 5 to 6. An unsymmetrical switching process, the finite rise time of the provided current and the not perfectly defined current sources were three factors to mention. Furthermore a leakage current were induced by the commutation time of the switching process. This distortion was mainly observed for low frequencies when the output capacitance was fully charged and discharged. In the higher frequency range this did not effect the integrity very much. As already mentioned in the design process, the circuit was designed to fulfil the requirement of synthesizing signals in high frequencies.

The signal frequency of 1 GHz represented a lower bound on the frequency range in the used configuration. The upper bound of the frequency range is limited to the detectable voltage swing of the amplitude. If a voltage swing of 2 V is still accepted, the upper bound

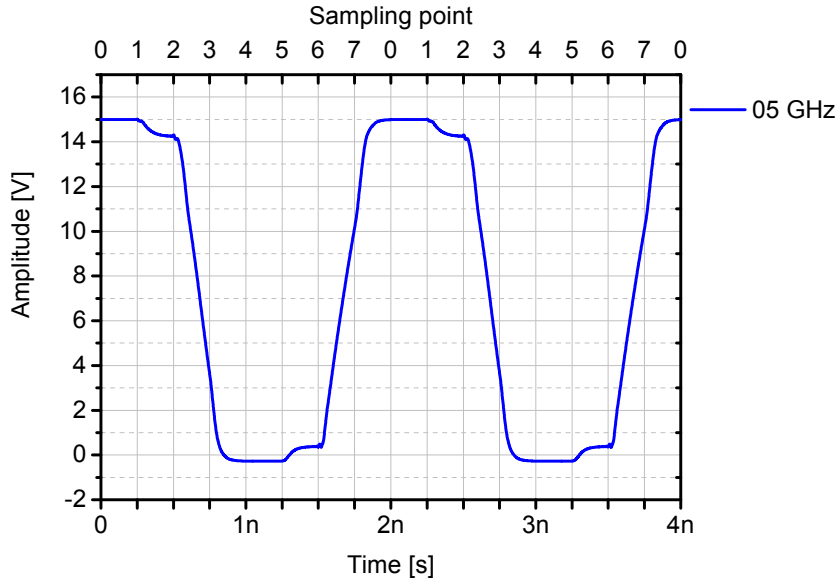


Fig. 4.3.: Synthesized sine wave for frequency of 0.5GHz

would be a signal frequency of 6 GHz with the presented Riemann Code. For lower voltage swings even higher frequencies could be reached. In the following the signal quality is compared in more detail. Assuming a sine wave of the form

$$v(t) = V_{DC} + \hat{v} \cdot \sin(2\pi f \cdot t + \phi), \quad (4.3)$$

Figure 4.4 illustrates the comparison of this theoretical sine wave (red) with the synthesized signal (black), taken from Figure 4.2, at the frequency of 1 GHz. The theoretical sine wave had an amplitude of $\hat{v} = 7.5$ V, a signal frequency of $f = 1$ GHz, a phase shift of approximately $\phi = \pi/4$ and an DC offset of $V_{DC} = 7.5$ V.

Although the synthesized signal is clipped and the mentioned distortion came into play, the shape looked like a sine wave. The SNR of the synthesized signal was calculated with MatLab and was $SNR = 15$ dB. For a first evaluation of the signal quality after digital-to-analog conversion, the spectra were compared. The spectrum of a time signal demonstrates the frequency portions which are present in the signal. As the spectrum of a clear sine wave only consist of a DC component and its first harmonic, it was easy to obtain a comparable quantity compared to the synthesized signal. Figure 4.5 highlights the difference between the synthesized and the theoretical sine wave form in more detail.

On the top left side the theoretical sine wave is plotted in time domain. Underneath of it the spectrum presented a frequency portion for the direct component at 0 Hz and a fundamental frequency portion at 1 GHz. The spectrum of the synthesized sine wave on the top right side demonstrates a few distortions at higher frequencies. Beside the direct

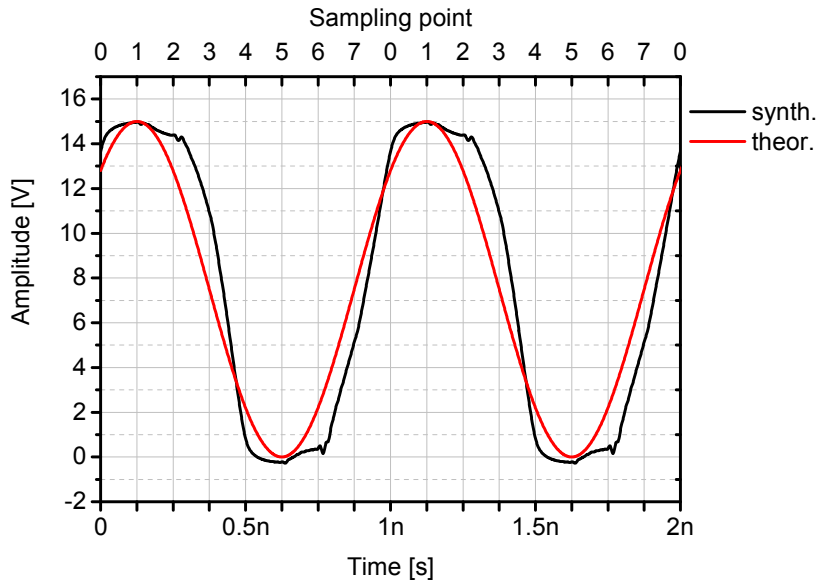


Fig. 4.4.: Synthesized sine wave with the theoretical sine wave

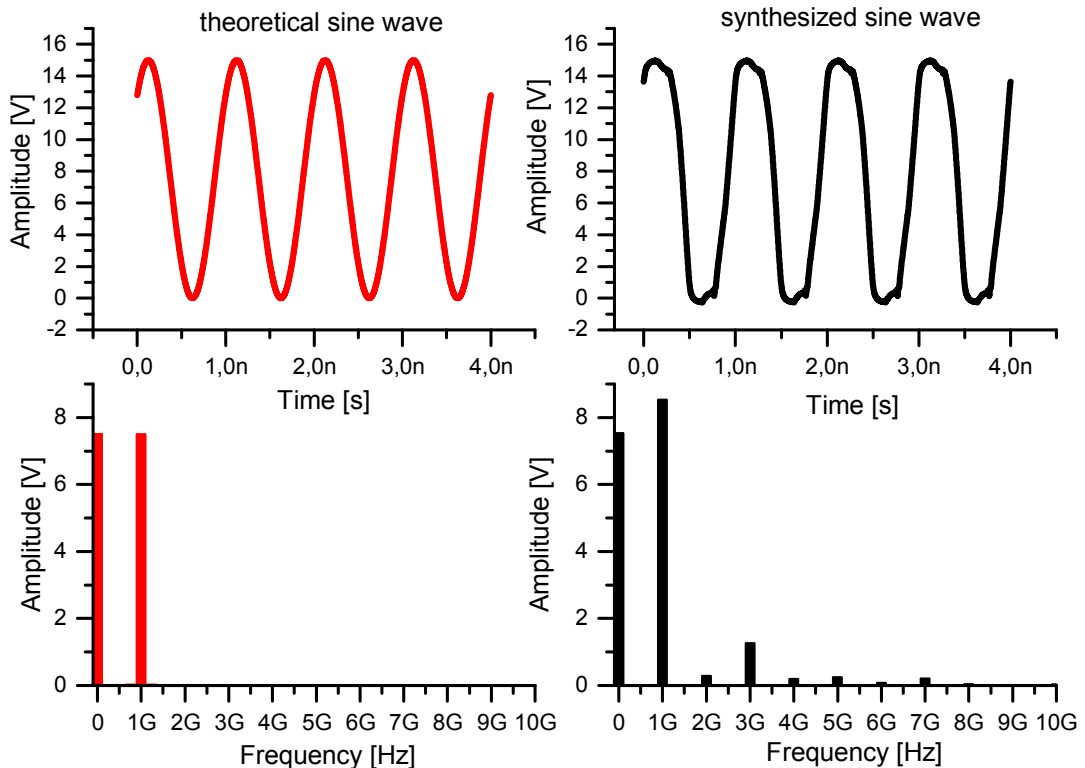


Fig. 4.5.: Comparison between a theoretical and a synthesized sine wave with their spectrum

and fundamental frequency component there were some additional unwanted frequency portions which distorted the signal. The comparison of the spectra was a good indicator for a first error estimation. This optical measure made it easy to evaluate the signal quality since the unwanted distortions were clear visible. At the third harmonic the signal deviates by 14% from the clear sine, as for the 2nd to 10th harmonic the deviation is up to 7%.

As already mentioned the calculated SNR was 15.2 dB of a theoretical achievable 27 dB, since this signal was scaled for the full scale. Compared to a full scale sine wave, a SNR of 22 dB could be achieved for a frequency of 1.5 GHz with the presented Riemann Code in equation 4.2. Figure 4.6 demonstrates this synthesized signal with its SNR.

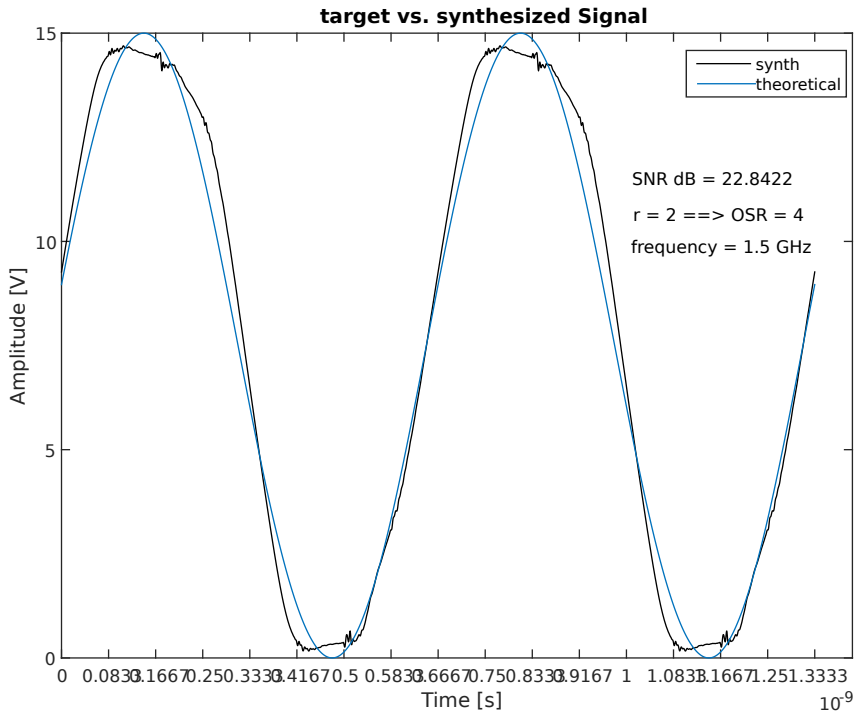


Fig. 4.6.: calculated SNR for frequency of 1.5 GHz

Further details on the SNR calculation for various signals, can be found in appendix E. In addition to tune the amplitude via the absolute sampling intervals, it was also possible to adapt the input control sequence, hence the sequence of chosen slopes to shape the output signal. The three bit resolution restricted the quantity of different slope combinations to six for synthesizing a sine wave. Considering only two sampling intervals to construct the rising edge of the positive half sine, the six combinations were: 75, 73, 71, 53, 51, .31 with respect to the i_0 values. As these relative slopes were used for the rising edge, the counterparts (negative values) represent the falling edge. The first digit indicated the slope of the first sampling interval and the second digit of the second, respectively. These six combinations were plotted in Figure 4.7 over two periods for the signal frequency of 3 GHz.

Here the effect of the Riemann Code became clear, since the change of the input control will also change the shape of the output signal. This was utilized to calculate the Riemann Code with an algorithm to fit the output to the desired signal. The algorithm had to be processed within the settling time of the DAC to ensure real time conversion.



Fig. 4.7.: Signals with the same signal bandwidth 3 GHz but different input control

4.1.2. Full wave rectified sine wave generation in the time domain

In addition to the sine wave, here a full wave rectified sine wave was simulated. Based on the same approximation principle as demonstrated in figure 4.1, the corresponding Riemann Code for the rectified sine was generated and is stated in equation 4.4.

$$000 \ 001 \ 010 \ 011 \ 100 \ 101 \ 110 \ 111. \quad (4.4)$$

As the rectified sine wave consisted only of the positive wave for a full period, the oversampling ratio is performed on half of a sine wave. This resulted in a more precise wave form which resulted in an OSR of eight ($r=3$) compared to the full sine wave. Here the number of slopes used for synthesizing the rising edge was doubled and hence four different slopes could be used. Therefore the rectified sine wave consisted of eight sampling points, while the corresponding positive half of a sine wave only consisted of four sampling points. The rectified sine wave exhibited the sequence of all eight different slopes, from the biggest positive to the biggest negative slope.

Signals in the frequency range of 500 MHz to 6 GHz were generated and are demonstrated in Figure 4.8.

The shapes of the signals with fundamental frequencies 2 GHz to 6 GHz fit very good to a rectified sine.. The issue of signal clipping was the same as mentioned earlier. This effect was seen in Figure 4.8 for the blue curve which had a fundamental frequency of 500 MHz. Further investigations on the SNR were omitted due to the limited scope of this thesis.

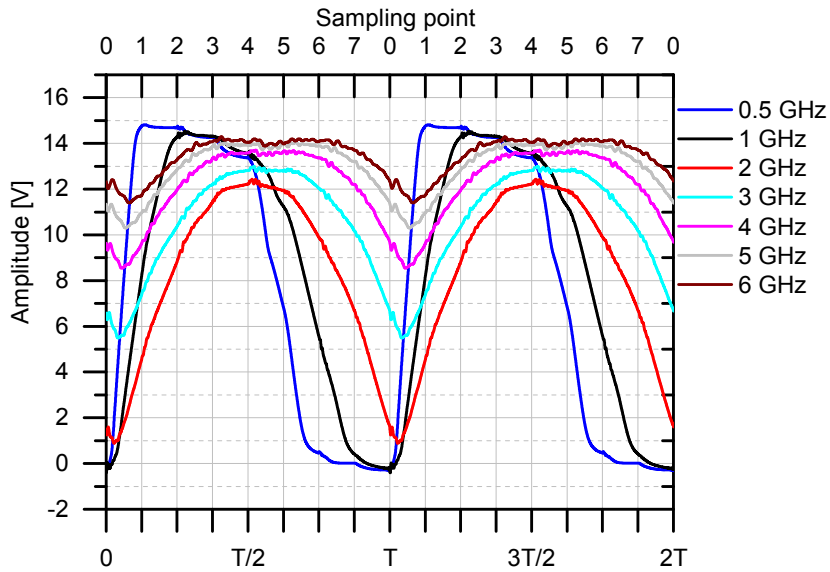


Fig. 4.8.: Signals with same slope but different signal bandwidth

4.1.3. Triangular wave generation in the time domain

As the designed circuit should act as a signal generator another signal was synthesized. A triangular signal was chosen to validate the feasibility of generating arbitrary waveforms. The wave form of a triangular signal is generated by charging and discharging a capacitor for the same period of time. All simulations so far, were run with a three bit resolution of the realised circuit. This three bit resolution represented eight different slopes and therefore for a equally charge and discharge process four different slopes could be used. These four slopes were $+7, +5, +3, +1$ for the charging process and their counterparts $-7, -5, -3, -1$ for discharging. Hence the sequences of slopes were: 77, 55, 33 and 11 with respect to i_0 values. Figure 4.9 demonstrates the four different combinations for synthesizing a triangular wave form for f_{signal} (signal frequency) = 2 GHz.

The fundamental frequency was set to 2 GHz representative for the signals with f_{signal} in the frequency range of 500 MHz to 6 GHz. In this configuration only the wave form for the biggest slope (77; cyan) deviates from the desired signal. At the sampling point 2 the output capacitance is fully charged which led to an undesirable signal form. In fact of the high current and long sampling interval, the output capacitor is fully charged. The problem of not defined reference currents can be observed in the following calculation. For a reference current i_0 of approximately 160 mA, a capacitance C of 20 pF and a sampling interval dt of 125 ps the voltage swing can be calculated as:

$$dU = \frac{7i_0 * 2dt}{C} = 14V, \quad (4.5)$$

which fit pretty good to the cyan signal in Figure 4.9. Taken the same parameters for the slope of $5i_0$ it follows a voltage swing of $dU = 10V$, $dU = 6V$ and $dU = 2V$

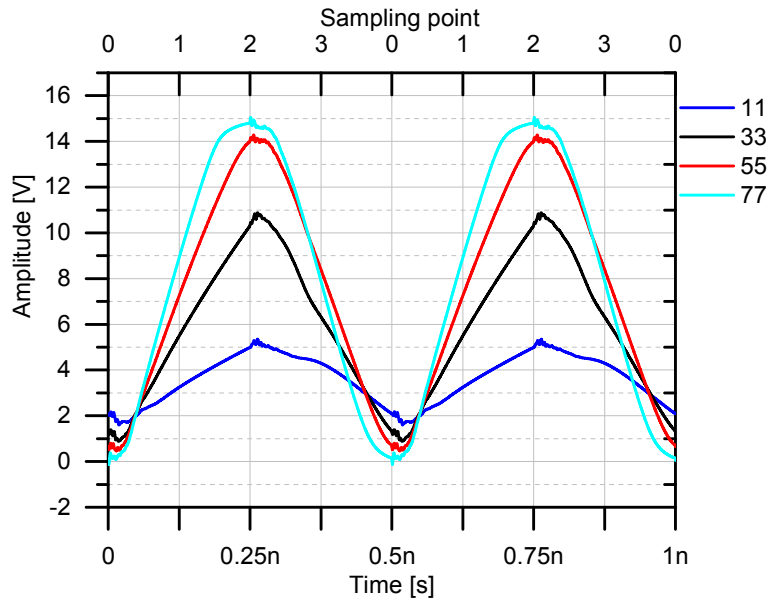


Fig. 4.9.: Triangular signal with same signal bandwidth but different slopes

respectively for $3i_0$ and $1i_0$. As mentioned earlier the problem of not perfectly defined current sources came into play, since this voltage swings could not be observed in Figure 4.9. Representative for the four combinations to synthesize this triangular signal waveform, Figure 4.10 demonstrates the frequency varying signals from 500 MHz to 6 GHz for a slope of 33.

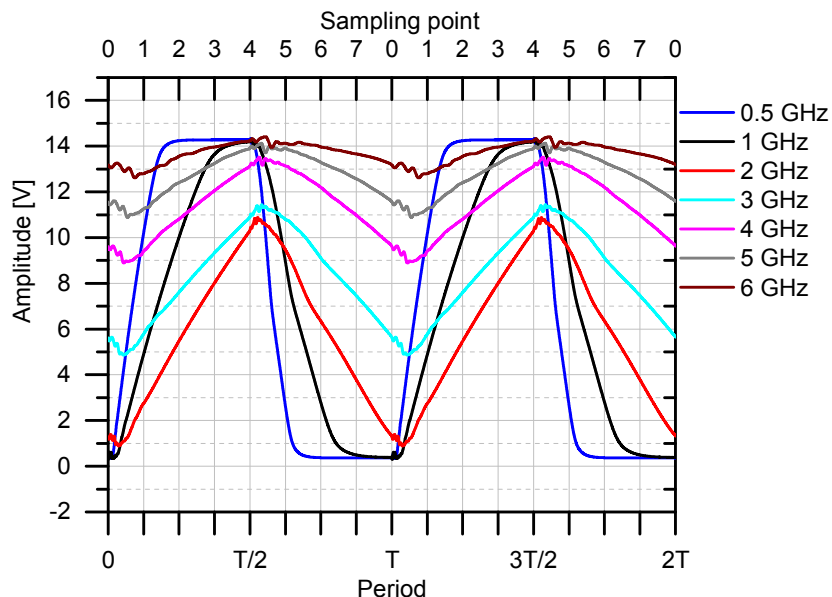


Fig. 4.10.: Triangular signal with same slope but different signal bandwidth 3GHz

4.2. Stability analysis of the realised circuit

To guarantee a proper function of the circuit a short stability analysis was performed. This analysis was necessary to check if the circuit oscillates. To prevent the circuit to take damage this oscillation had to be avoided. It was checked if the DUT (device under test) was stable for the whole frequency range used. Using a S-parameter simulation the complex impedance at various critical points was calculated. One condition to start an oscillation is a feedback path which existed for the designed circuit. The driver circuit for the high side switch is connected to the output and hence the feedback is established. To avoid unwanted oscillation the real part of the complex impedance had to be positive for the whole frequency range. A basic definition of passive elements were that they have a reflection coefficient magnitude less than unity. Checking the input reflection coefficient, the values had to be inside the unity circle. Therefore no negative resistance would be allowed to occur since that can lead to unwanted amplification and oscillation which can damage the circuit [19]. Because the real part of the impedance at all measurement points were positive for the whole frequency range, the circuit seemed to be stable. The stability check was performed within the ADS tool.

4.3. Power consumption analysis of the realised circuit

As the concept is designed for the purpose to implement in mobile communication systems the power consumption is crucial. Since the energy storage of mobile devices is limited, it is important to get a decent power dissipation for the test circuit. A short analysis should give an insight to the expected power consumption of the designed test circuit. Due to the expected switching losses [18]:

$$P_{sw} = \frac{1}{2}V_{in}I_0(t_{on} + t_{off})f_{sw} \propto f_{sw} \quad (4.6)$$

the power consumption scales linear with the switching frequency, here $f_{sampling}$. Simulations confirmed this assumption for switching the smallest bit of the Riemann Pump. The used input code was a sequence of alternating bits, since its a different power consumption for switching $+1i_0$ than for $-1i_0$. Switching the high side transistor to the off state results in a leakage current over the high sides driver circuit. A trade off between switching speed and power consumption resulted. For an increase in the switching speed, hence an increase of the signal bandwidth, the power consumption also linearly increase. In addition to this, the power consumption of the driver circuit also increases with the switching speed, as

the dimensions of the used components have to be adapted. The used driver circuit was optimized to reduce the power consumption for a maximum frequency of 100 MHz, as it was implemented in a power application system [15]. In Table 4.1 the losses are illustrated with the corresponding sampling (switching) frequency of the used configuration.

Table 4.1.: Overall power losses for sampling rate

$f_{sampling}$ [GHz]	P_{diss} [W]
4	3.982
8	4.259
16	4.778
24	5.011
32	5.144
40	5.264
48	5.354

The used configuration referred to the one bit Riemann Pump consisted of two power transistors, for the high and low side switch, with a gate periphery of 800 μm , four driver transistors each with 200 μm gate periphery and the bias voltages of $V_{dn} = -5 \text{ V}$, $V_{dp} = 0 \text{ V}$ and $V_{dd} = 15 \text{ V}$. This configuration can be seen in appendix A on the right hand side.

4.4. Proof of concept simulation with existing components

In the last step a simulation was run which made the concept comparable to the realized circuit. The realized circuit was designed with the help of former designed chips. In this simulation the transistor dimensions were adapted to the dimension of the built demonstrator. This should give an insight to the behaviour of the constructed demonstrator. The detailed modelling and simulation of the designed circuit under real conditions, considering all loss effects would go beyond the scope of this thesis, since no models for the used chips were available. As the realized demonstrator differs slightly from the presented concept, Figure 4.11 demonstrates the circuit schematic for one bit.

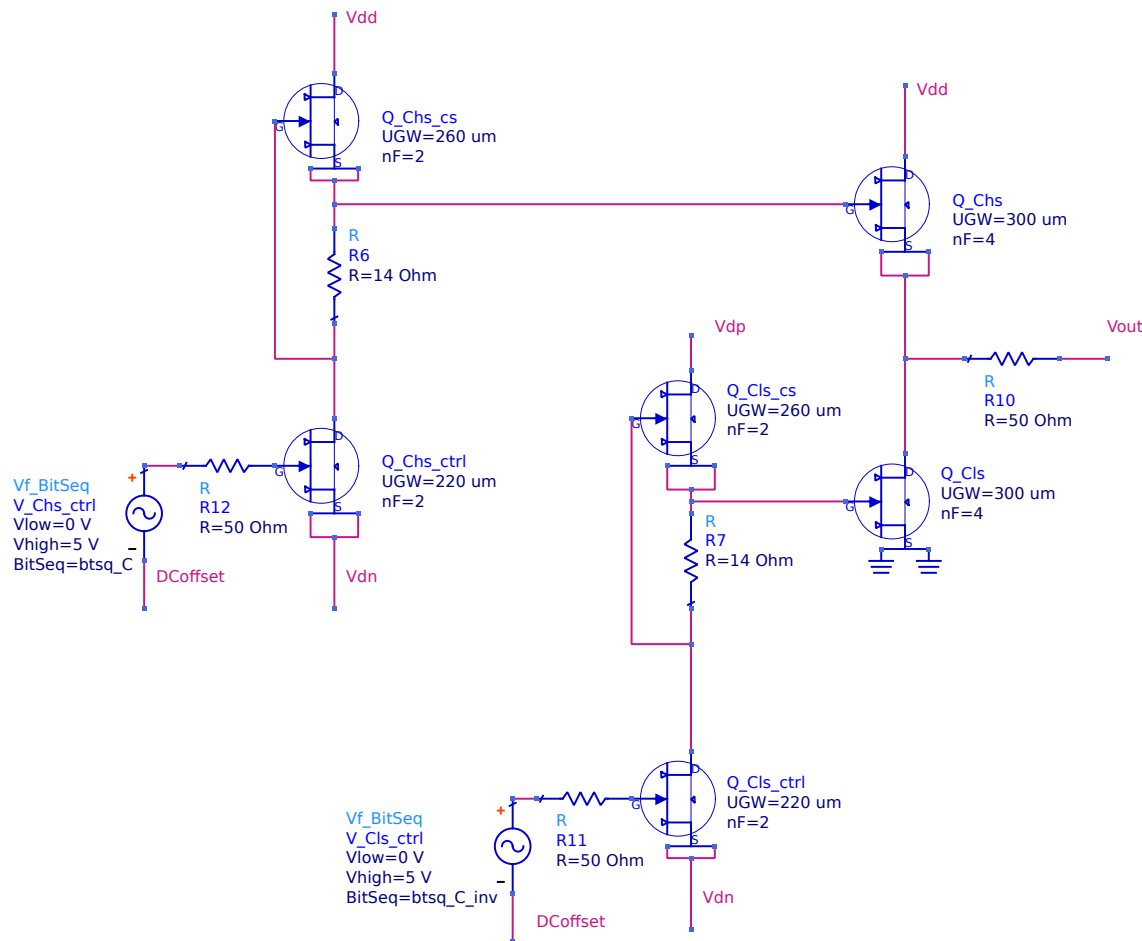


Fig. 4.11.: demo circuit

The difference to the presented concept was that no feedback path from the output to the drain of the high side driver circuit existed. The result of this was that the efficiency was not as good as for the presented concept in chapter 3. It is to mention that the transistors for the other bit scales with the factor 2. The full schematic of the built demonstrator circuit

can be seen in Appendix B. Although the used chips for the demonstrator were designed in a former work, no simulation files were available which made a detailed simulation difficult. Nevertheless this built circuit acted as expected and a signal could be synthesized, as seen in Figure 4.12.

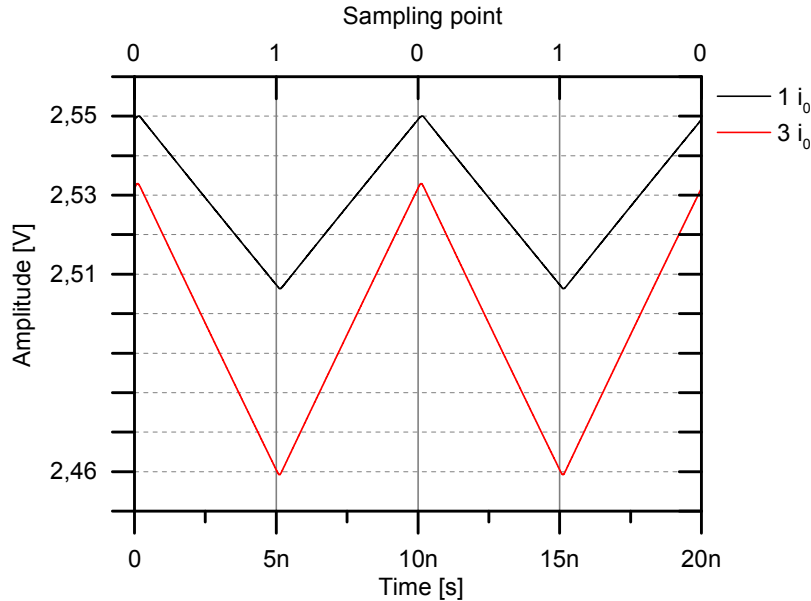


Fig. 4.12.: Simulation result for the output voltage using the realized components

As the measurement of the time signal was performed with an oscilloscope and a probe, the load impedance differs from the concept. Figure 6.5 in Chapter 6.4 presents the equivalent circuit for the measurement. Considering this, gave the simulation results presented in Figure 4.12 which demonstrates the signal generation. The black signal represents a triangular waveform with a relative slope of $1i_0$ and the red of $3i_0$, respectively. The voltage swing is $0.04V$ and $0.07V$ since the probe divides the real voltage with a ratio of 10:1 to avoid any damage of the oscilloscope. Therefore the real voltage swing is $0.4V$ and $0.7V$ which fit pretty good to the measured data in chapter 6.4. The simulation is run with the circuit in Figure 4.11, a load impedance corresponding to the measurement in Figure 6.5 in Chapter 6.4, $f_{sampling}$ of 200 MHz and $V_{dn} = -5V$, $V_{dp} = 0V$, $V_{dd} = 5V$.

4.5. Evaluation of the simulation results for the Riemann Pump

Different wave forms could be synthesized (sine wave, rectified sine, triangular). The dimension of the used components already limits the bandwidth. To shift the bandwidth to higher values the transistor dimension have to be bigger and smaller to shift to lower values, respectively. The signal frequency of 1 GHz represented a lower bound on the frequency range in the used configuration. With an OSR of four $f_{sampling}$ is eight times f_{signal} . The smallest achievable current times the smallest sampling time (highest sampling frequency) determine the smallest voltage step achievable. If the OSR is increased, the sampling time is decreased and therefore the signal quality is better because we have a more accurate synthesized signal. The upper bound of the frequency range is limited to the detectable voltage swing of the amplitude. In addition to this the components have a unity current gain frequency limit. Higher frequency means much lower sampling time which can lead to non detectable voltage steps (slopes are not detectable). Parasitic and loss effects distorted the waveforms. Since the digital to analog conversion always introduces noise to the signal the fit was not perfect. The highest SNR (32.5 dB) found was for a sine wave at 6 GHz with an amplitude of $\hat{v} = 1.75V$, an DC-offset of $V_{DC} = 13V$ and a phase shift of $\phi = -\pi/8$, see appendix E. There are the SNR values presented for the seven different signals of Figure 4.2 with their corresponding theoretical wave form parameters. The system is stable. The stability check was needed to validate that the circuit did not oscillate. The energy consumption is in the range for base stations and have not reached it yet for mobile devices. Since the resolution should be in the range of 17 bits. If the resolution is increased to get a better accuracy, the whole circuit would become more complex and the energy consumption would increase. If the OSR is increased to get a better accuracy, the switching frequency is also increased and therefore the energy consumption. For high switching frequencies the switches have to switch within a few ns which increase the gate drive current which increase the power loss. This is the trade off between the shift of the bandwidth (shifting to even higher frequencies is possible but the bandwidth is nearly constant) and power consumption. The designed test circuit is not optimal with respect to efficiency. The implemented driver circuit absorbed unexpected leakage currents.

Nevertheless the simulation results confirmed the feasibility of the chosen approach. Some trade-offs in mind and the ability to change some system parameter made it possible to generate some good fitted signal waveforms.

5. Realisation of a demonstrator

The demonstrators realized in this work consisted of several MMIC (microwave monolithic integrated circuit) chips with a filter network built by discrete elements. Due to the fact that SMD (surface mounted device) decoupling capacitors as well as MMIC were used, this were called hybrid test circuit. For assembling and measurement purposes the test circuit was restricted to a resolution of two bit. Otherwise the bonding, assembling and controlling of the inputs would became too complex. Two bit resolution implied to create an input control strategy for the four inputs. A third bit of resolution would enhance the performance but also increase the complexity of the realisation as six inputs needed to be controlled.

A two layer high frequency substrate, namely Rogers RO4003, were used. The benefit of the low dissipation factor, a low tolerance of dielectric coefficient and the stable electrical properties made this the most suitable material for the broadband application.

With the help of former designed chips, two different versions of the substrate were designed. To make use of these chips it was necessary to design two different versions due to the different properties of the chips. The two layer substrates were ordered with a thickness of 0.508 mm, a 35 µm Cu conduction layer and a ChemNiPdAu metallisation. An impedance control ensured the correct impedance of 50Ω for the 1.1 mm wide MSL (microstrip line) at the in- and output of the circuit.

Each version of the designed substrates had the size of 60 mm x 54 mm while the area for the multi assembled chips covered approximately 6 mm x 5.5 mm for both. One layout was designed for chips which ground contact were plated through the backside metallization of the chip. Yielding a power transistors source contact connected to these ground plates. This property yielded a great drawback compared to the other layout.

The second layout of the substrate were planned to improve the heat transfer by using another type of chip. This chips ground contact were not plated through the backside metallization, making them suitable for soldering on a conducting heat spreader.

To make use of the former designed chips, these two layouts were designed to enable the proof of concept.

5.1. Substrate layout using DDRi_X6 and DDRi_Y6 chips

The presented layout of the substrate was designed for the use of the chips DDRi_X6 and DDRi_Y6 since the chip DDRi_2C required a different multi chip connection. Figure 5.1 shows the overview of the designed substrate, consisting of a decoupling capacitor network, several dc voltage and RF connectors and the core of the circuit.

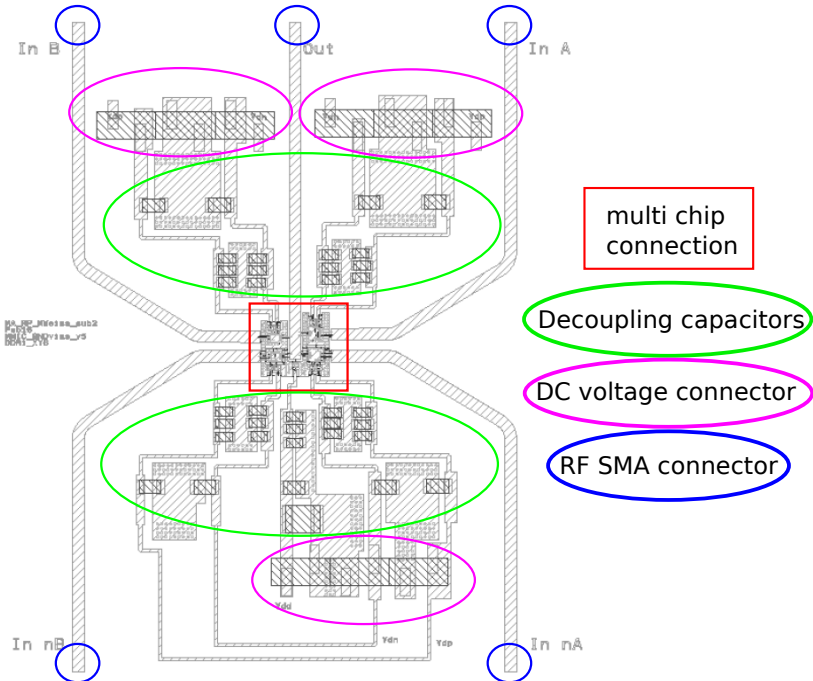


Fig. 5.1.: Layout substrate with DDRi_XY6 chips

It is to mention that the layout outside the red marked box was very similar for the others version. So one explanation of the layout outside the box were sufficient. Only one additional DC voltage supply line was added and the arrangement of the chips were different. Due to the different arrangement of the chips attention was paid to the connection of bias voltages.

The described part outside the red box consists of the SMD decoupling capacitor filter network and the multi pin connector for the DC voltage supply. In addition to this the in- and output transmission lines were designed to fit to an 50Ω impedance.

The decoupling capacitors, also known as bypass capacitors, filtered out undesired frequency portions by the power supply. If the filter network did not work properly, this could lead to undesired oscillations of the circuit. Following a very common design rule lead to the right choice of capacitors. A very first decoupling capacitor was integrated on the MMIC chip. The requirement to place the decoupling capacitors as close as possible to the DC voltage supply pad lead to the choice of a special MMIC capacitor. It was

possible to place that capacitor as near as possible to the chip to keep the length of the bonds small. To avoid resonance peaking the most suitable capacitors were those with a high ESR (equivalent series resistance) since the quality factor of these were small. A great bypassing range were enabled by choosing a 82 pF capacitor, namely D20BT820K5PX from Dielectric Laboratories Inc., to filter out frequencies in the GHz range. The gold metallization (for wire bonding), the thin film technology and the custom sizes (to keep it small), made this the most suitable capacitor for the purpose filtering high frequencies. Each capacity, of subsequent capacitors, were increased by one order in magnitude yielding the biggest capacity of 10 μ F. The big capacity filtered out frequency portions in the lower kHz range. In addition to the capacity also the temperature and voltage range had to fit. The following choice for the capacities was taken: 82 pF, 1 nF, 10 nF, 100 nF, 1 μ F, 10 μ F, started at the chips supply pin.

In fact that oscillation still could appear, the size of the used pads was designed larger, making it possible to change (adapt) the capacities for the filter network. These pads also had some via holes to transfer the ambient temperature to the backside. This was the attempt to keep as much as possible heat away from the chips.

The four input lines, as well as the output line, were designed to fit to an impedance of $50\ \Omega$. With a line calculator, namely line calc in the program ads, the corresponding line width was calculated. The calculated width of the line was 1.1 mm which was checked by the manufacturer with an impedance control as well.

The arrangement of the chips was realised to keep the length of the bond wires as short as possible. However the distances between conduction lines were limited by the process of the manufacturer. The transmission lines of the signal path were designed to fit each other. All transmission lines were matched to $50\ \Omega$ and got the same length to avoid undesired delays of the signal. An important fact to consider was that all switches had to switch synchronous at the same time. Therefore no signal delays were permitted, induced by different transmission lines.

The assembly of the multi chip connection marked with the red rectangular is described in Figure 5.2.

The drawback of these chosen chips were its plated through ground contact. In fact of this, a proper function of these chips as a high side switch, made it necessary to place it on an electrical isolated pad. At the bottom of Figure 5.2 these chips were placed on an isolated pad. This pad did not have any connection to the backside potential of the substrate. The pads were surrounded by a large conducting layer with via holes to spread the heat. The idea was to dissipate the heat over the air bridge, through the via holes of the conducting layer, to the backside of the substrate. The substrate was mounted on a beam(?), which improved the cooling a little bit. The beam was necessary to install the

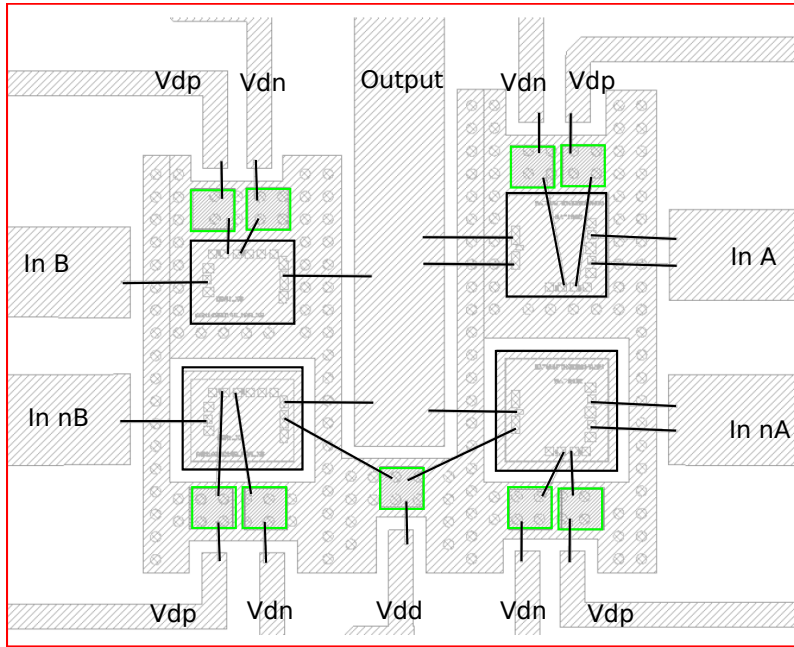


Fig. 5.2.: Layout DDRi_X6 and DDRi_Y6 chips

RF-SMA connectors and therefore the connection between the circuit and the measurement equipment. This was a very critical design issue since the chips created much power, hence much heat.

As mentioned earlier the length of the bond wires were set to be equal for the signal paths. Since an in-phase control of the input was important to ensure the switches to turn on/off synchronous. The length of the bond wires providing the DC voltage supply were not critical. The diameter of the wedged Au (aurum; Gold) bond wires was set to 25 μm which ensured a maximum current of approximated 1 A for a bond length of 1 mm. The small diameter and the short length made it most suitable for the high frequency application.

Figure 5.3 shows the assembling of the used chips with their corresponding bond wires. As mentioned the bond wires got the same length for the signal path.

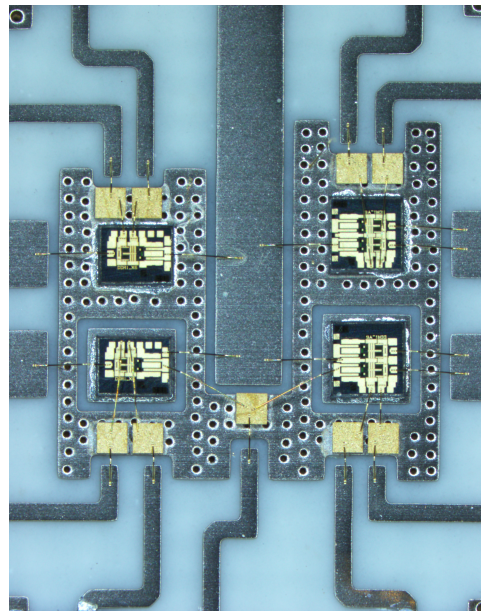


Fig. 5.3.: Photograph of assembled DDRi_X6 & DDRi_Y6 chips

5.2. Substrate layout using DDRi_2C chips

The layout of the filter network and the DC supply voltage did not differ as much from the previous presented layout version. In this second layout one additional DC connector was added and the arrangement of the chips differed. Figure 5.4 shows the arrangement of the used chips, namely DDRi_2C.

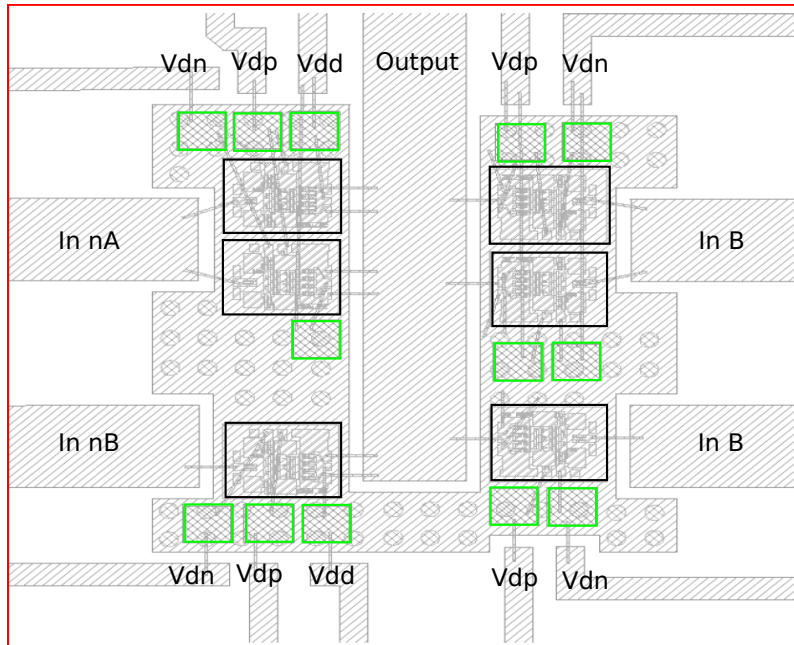


Fig. 5.4.: Layout DDRi_2C chips

Due to the fact that six chips were used in this layout, the wiring of bonds was more

complex. Also the placement of the high and low side switches differed in contrast to the previous layout. The switches, representing one bit of resolution, were placed horizontally while the previous layout showed the switches placed vertically. Horizontal alignment was chosen due to easier bond wiring. This led to a different bias voltage connections.

The most important difference in the two layouts were the difference of used chips. The chips used in this layout version, DDRi_2C chips did not have a plated through hole to its backside. Thus, these chips could be soldered directly to the heat spreading backside connected layer. The heat could transfer directly from the backside of the chip through the via holes to the substrates backside. This improved the heat transfer a lot in contrast to the first design. It must be pointed out to connect the ground potential of the chips separately to the boards ground potential. This version might work better due to the better heat dissipation, although the fabrication of the chips was older (2011).

The assembled chips for the second version is shown in Figure 5.5.

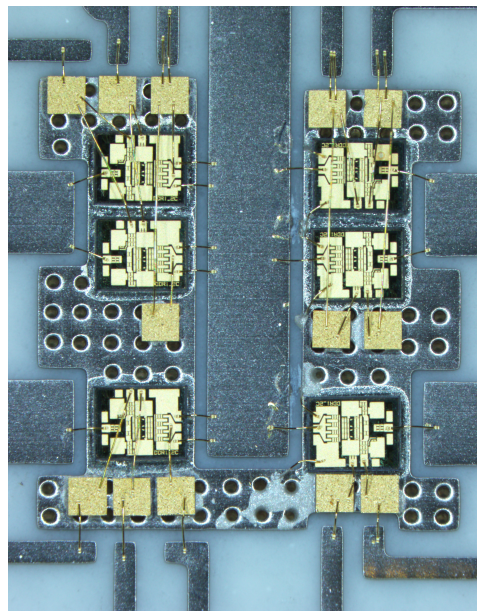


Fig. 5.5.: Photograph of assembled DDRi_2C chips

5.3. Evaluation of the design and realisation process

In the realisation and layout process many things had to be considered.

The circuit was built on a hybrid assembly which combines the MMIC with the discrete SMD components on a Rogers 4003 substrate.

The input and output lines on the substrate were MSL which were matched to 50Ω . Important for the design of the input lines were that they are of the same length, due to timing issues. The input timing is crucial due to the fact that the switches have to switch synchronous. The output line was matched to 50Ω to ensure proper measuring.

In addition to the same length of the input lines, also the bond wires of the in- and output to the MMIC chips had to be of the same length. One of the most important and crucial things was the dissipation of heat. Based on the designed chips, two different concepts were chosen to dissipate the heat in the most proper way.

The wafer run of the chips DDRi_2C was from the year 2011 and therefore five years old and hence the taping of the wafer could be not as good as the newer ones.

For bonding $25\mu\text{m}$ (diameter) Au bonds were used. The length of the bonds were given by assembly limits for spacing of conducting layers due to manufacturer process limits.

In- and output connectors were commercially available SMA jack connectors with a matched impedance of 50Ω to connect standard RF cables.

The two layouts were fabricated by CONTAG AG while the needed components were ordered at Digi-Key Electronics.

The finished demonstrator is shown in Figure 5.6 with a short description of the placed elements.

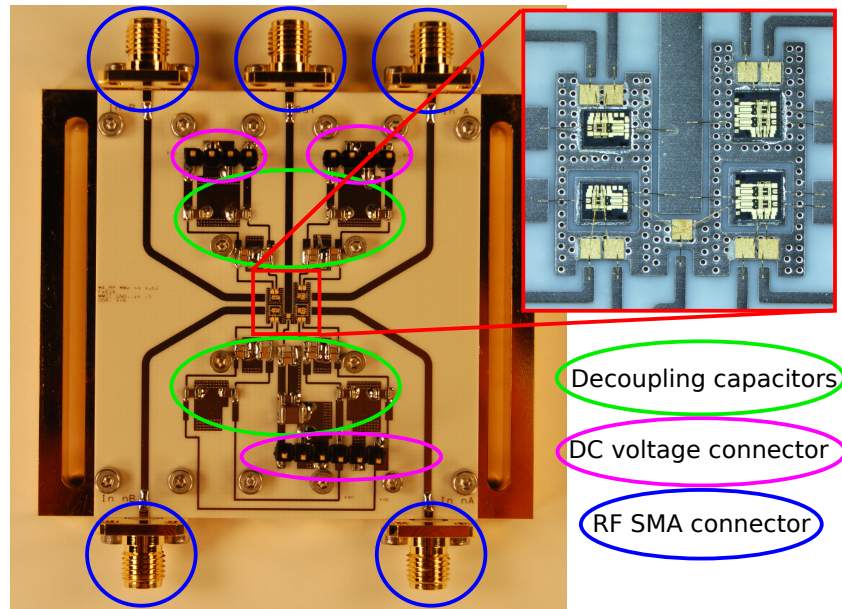


Fig. 5.6.: Assembled demonstrator

An improvement for the layout, could be to solder the DDRi_XY6 chips on an electrical insulator while thermal good conductor, as AluminiumNitrid (AlN: 180-200 W/mK -> datasheet). This is needed to ensure the isolation from the output port to ground potential, but still have a good thermal transfer. This approach would have required only a small amount of the material AlN, which had to be cut very precisely into very tiny pieces, since the size of the chips DDRi_X6 and DDRi_Y6 were 1.25 mm x 1 mm and 1.25 mm x 1.25 mm, respectively. This pads adhered or soldered to the conduction layer ensure a good heat transfer.

In fact of the very small and precise size of the special material this was too costly for a first prototype to proof the concept.

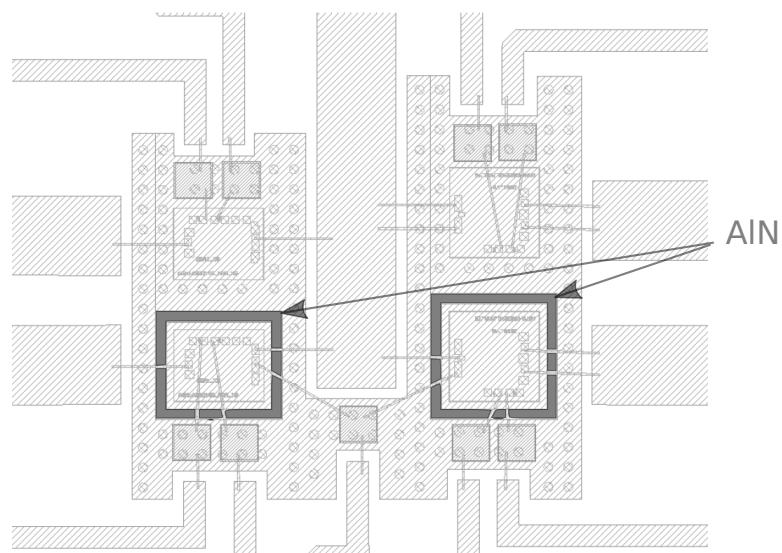


Fig. 5.7.: Improved layout for Chips DDRi_X6 and DDRi_Y6

6. Measurement of the realized circuit in the time domain

The aim of the measurement was to show the generation of different signals.

With respect to produce a decent signal waveform at the output, the assembled hybrid test circuit was terminated with a $50\ \Omega$ termination and a 3.3 nF capacitance, respectively. In contrast to the calculated capacitance of 20 pF in chapter 3, a over dimensioned capacitor of 3.3 nF terminated the output to ensure that the signal would not be clipped.

After the calibration of the measurement instruments a stability check was performed to ensure that the test circuit do not oscillate. In a next step the output of the circuit was measured with a resistive load to show the function of the push-pull stage. The correct functioning of the push-pull stage enabled the measurement with a capacitive load to synthesize a triangular waveform. In order to avoid any kind of damage the measurement was performed with low DC supply voltages.

6.1. Measurement setup

An overview of the measurement setup is given in Figure 6.1.

A signal generator generated a square wave signal with an amplitude of 0.7 V and 0.45 V , respectively. As a square wave signal consists of several harmonics, the pre amplifier had to support a wide bandwidth.

The square wave of $Ch1$ & $\overline{Ch1}$ and $Ch2$ & $\overline{Ch2}$ of the AWG (arbitrary waveform generator) is amplified by broadband amplifier G1 and G2, respectively.

A DC bias voltage is applied to the inputs of the DUT to generate a square wave signal from $V_{low} = -10\text{ V}$ to $V_{high} = -5\text{ V}$. The voltage swing of 5 V as well as the DC bias voltage were needed to ensure that the input transistors switch completely on and off. Several power supplies provided the necessary DC supply voltages for the broadband amplifiers, bias tees and DUT.

For the measurement of the push-pull stage an attenuator with 20 dB attenuation was connected between the output of the DUT and the input of the oscilloscope. This attenuator ensured that the specifications of the oscilloscope (scope 1) were complied.

The measurement of the voltage across the load capacitance was done by another oscilloscope (scope 2) which provides a handy probe. This probe allowed to measure the voltage

directly on the output line of the hybrid test circuit.

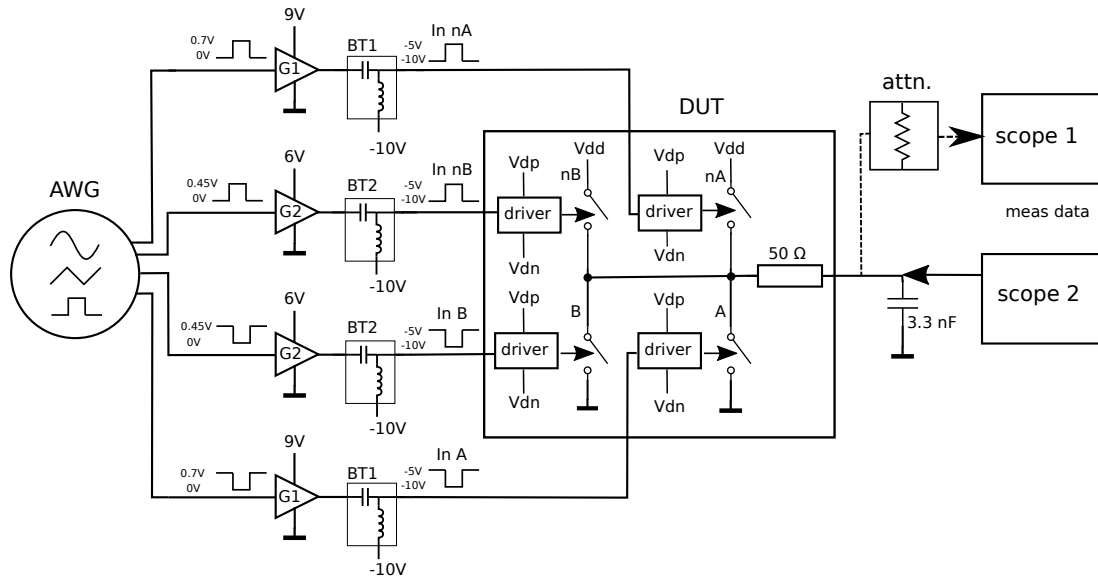


Fig. 6.1.: Schematic of time domain measurement setup

The elements of the measurement setup were:

- Signal generator: Keysight M8195A AWG
 - Ch1 & $\overline{Ch1}$: $V_{p-p} = 0.7 \text{ V}$ (square wave)
 - Ch2 & $\overline{Ch2}$: $V_{p-p} = 0.45 \text{ V}$ (square wave)
- Broadband Amplifier
 - G1: SHF803
gain = 17 dB (typ.), B = 35 kHz - 40 GHz
 - G2: SHF804TL
gain = 21 dB (typ.), B = 200 kHz - 55 GHz
- Bias Tee
 - BT1: SHF121A
B = 50 kHz - 65 GHz
 - BT2: SHF121D
B = 50 kHz - 65 GHz
- DUT
- Power supplies
- Attenuator: 18B50W
B = DC - 18 GHz, Attenuation = 20 dB
- Capacitive load

ceramic SMD capacitor (3.3 nF)

- Oscilloscope
 - scope 1: DCA-X 86100D + 86118A (module)
 - scope 2: DSO-X 3034A + HP 10432A (probe)

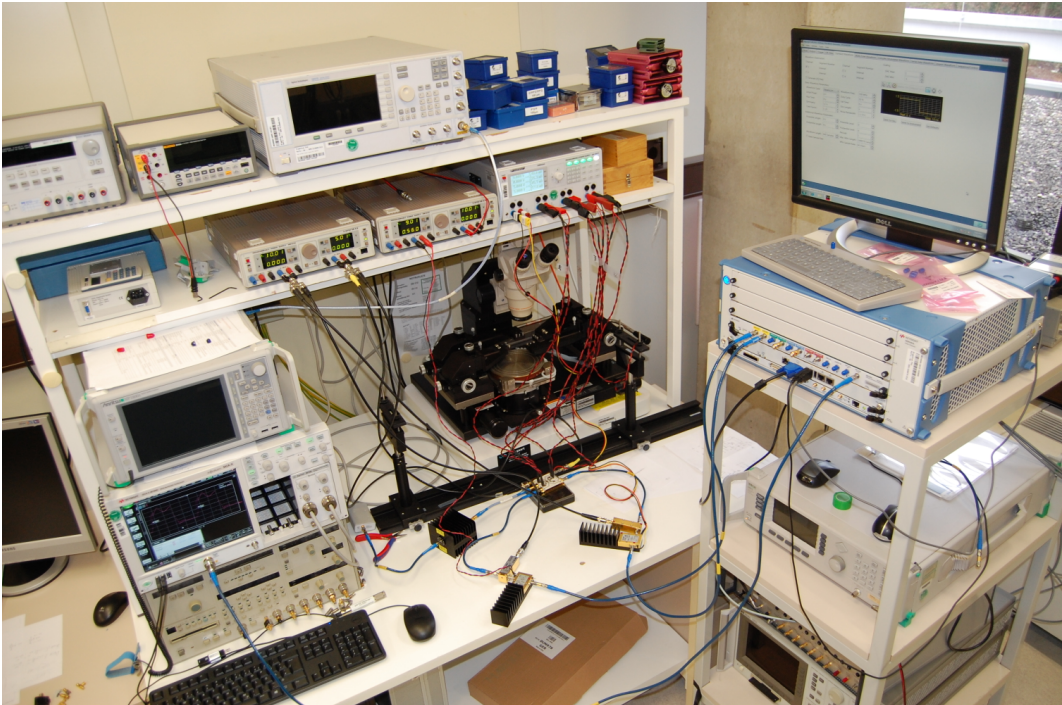


Fig. 6.2.: Photograph of measurement setup

6.2. Calibration and stability check

Before performing the first measurement the instruments and used devices had to be calibrated. The AWG output amplitude had to be adjusted to the proper value depending on which pre amplifier is used, as the broadband amplifier differ in their gain. The actual broadband amplifiers gain has to be checked as well as the proper configuration of the bias voltages. These prerequisites are necessary to ensure a proper measurement. After the calibration the first measurement checked the stability of the circuit. Therefore the DUT was supplied with its bias voltages and than the current was checked if it stays constant. Due to the fact that the current was stabilized after the transient time, it showed that the circuit is stable. For this measurement the in- and output connectors were terminated with $50\ \Omega$ terminations.

Simulation yielded a power consumption of 1.29 W for the one-bit configuration using the smaller push pull stage. This push pull stage is marked in the schematic in appendix B

with C and can be seen on the right side for landscape orientation of the schematic. This smaller push pull stage refers to the stage B for the designed layout.

6.3. Time domain measurement of push-pull stage

After checking stability of the DUT a small signal is fed to its input. Feeding a square wave signal (digital signal) to the input of the device its output switches between V_{dd} and GND potential. This is done with the push-pull stage realized with multi chip assembling on a hybrid board. *The hybrid board consists of four inputs which two are working in differential mode.*

Switching the output to V_{dd} needed an in phase control signal. Two high side transistors should switch and feed the upper power rail which is V_{dd} to the output. Meaning both power transistors have to switch at the same time to provide V_{dd} to the output. While highside and lowside transistor both switched on the output is floating between V_{dd} and GND.

Figure 6.3 shows the square wave input control signal. The square wave signal form represents a digital signal with a data rate of 200Mbps while the fundamental analog frequency is at 100 MHz. The required peak to peak voltage is configured to be 0.7 V. The light grey signal represents one input stream while the darker grey signal represents the inverse one. This signal represents a digital bit stream which is needed to control the circuit. The data rate of the presented signal is 200 Mbps while the analog fundamental frequency is 100 MHz.

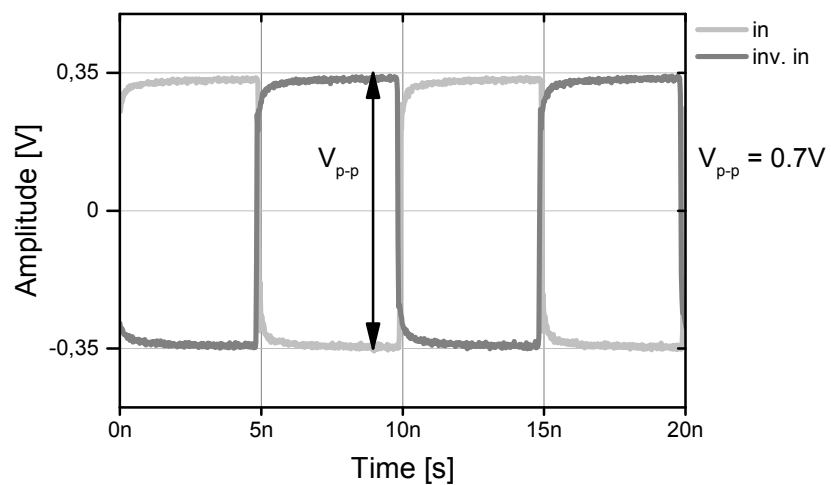


Fig. 6.3.: time domain measurement input control voltage

Using this input signal the circuit under test, with a 50Ω termination, provides the output shown in figure 6.4.

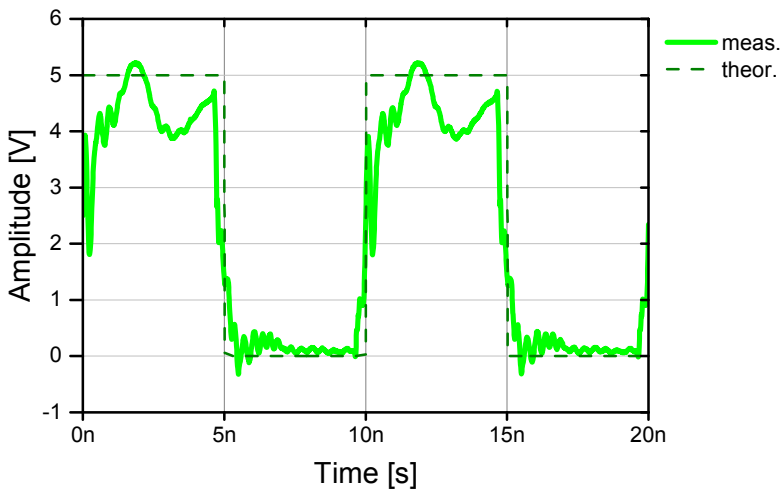


Fig. 6.4.: Time domain measurement of output voltage with 50 Ohm termination

The light green signal is the measured data while the dashed line describes the ideal behaviour. In an ideal world there would be neither rising nor falling time and the signal would switch between logical one and zero.

This figure demonstrate the proper functioning of the presented output push-pull stage, as the signal switches between Vdd and GND. In addition to this it is demonstrated that the switches are very fast since the rising and falling edges are very steep. The frequency accords with the input signal shown in figure 6.3.

6.4. Time domain measurement of synthesized signal

The purpose was to show if the designed circuit could generate different signals. Therefore it was to show if both bits of the circuit could switch synchronously. The equivalent circuit for the measurement with the oscilloscope and a probe head is demonstrated in Figure 6.5.

The proper functioning of the designed circuit led to verifying that both bits work together. If both bits work concurrently, it is possible to synthesize a signal. This proofs the concept and the chosen approach. The two bit resolution restricts the output voltage waveform.

In Figure 6.6 two different signals are shown which could be synthesized. The frequency of the synthesized triangular signal is 100 MHz while the voltage swing is 1.8 V and 0.8 V respectively.

The red signal represents a synthesized triangular waveform with a slope corresponding to $3i_0$, while the brown dashed signal provides the theoretical signal.

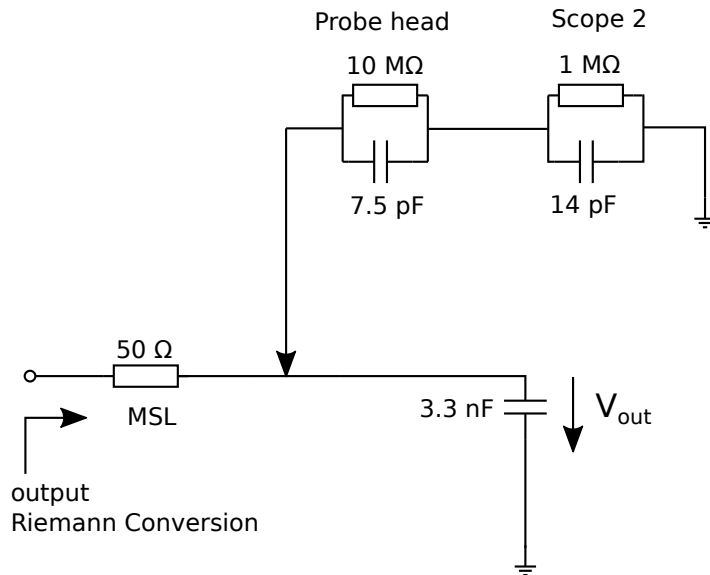


Fig. 6.5.: equivalent circuit of the time domain measurement

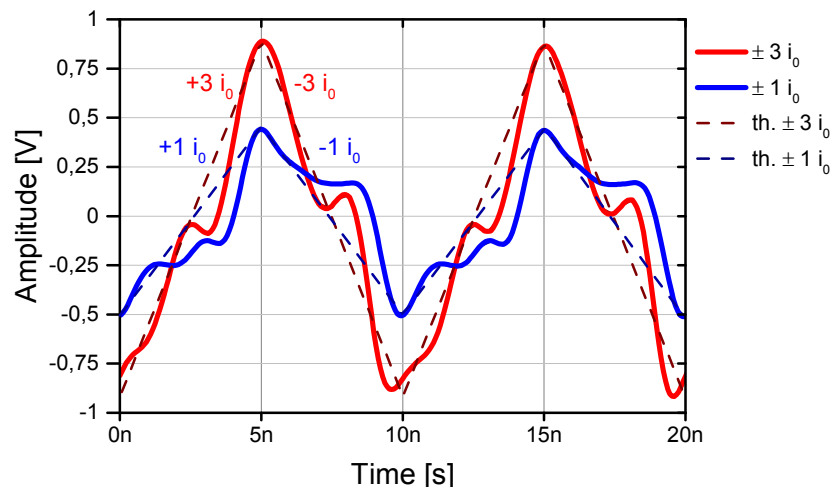


Fig. 6.6.: time domain measurement with capacitive load at $f_s = 100\text{MHz}$

The blue signal represents a synthesized triangular waveform with a slope corresponding to $1i_0$, while the dashed darker blue signal provides the theoretical one.

The same notation is valid for the synthesized signal in figure 6.7. Here the signal frequency is 150 MHz which is the upper bound for this measurement setup. The signal integrity is much worse going beyond this frequency.

The difference between the slopes is getting smaller while the signal quality is decreasing.

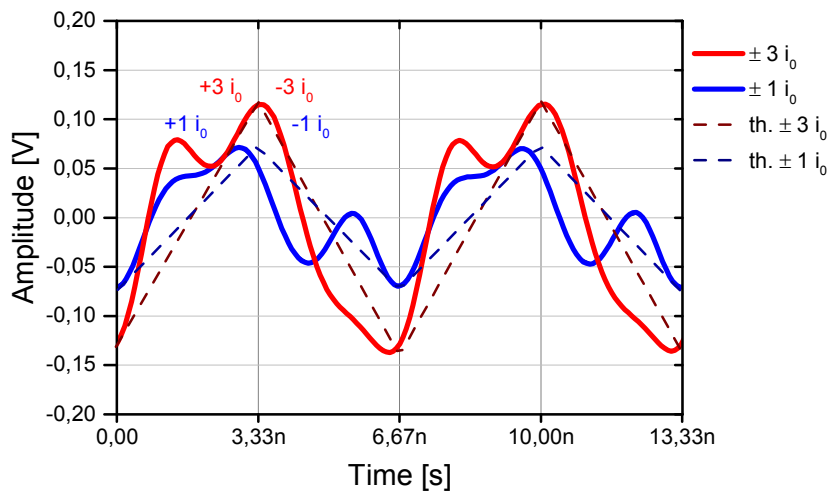


Fig. 6.7.: time domain measurement with capacitive load at $f_s = 150\text{MHz}$

6.5. Discussion of measurement results

In a first step it was shown that the designed circuit converts a digital signal to an analog one. The frequency limit for this measurement setup consisting of this designed circuit is at roughly 150 MHz. Heat is critical. Aside from some parasitic effects the proof of the concept was successful.

7. Conclusions and outlook

The implementation of the Riemann Pump in a system design has been presented. The design process from a charge pump to a custom DAC has been described. In contrast to classical current steering topologies this concept used the benefit of differential coding, which saves energy and exhibits a better performance. A concise evaluation states that the Riemann Pump is a great improvement for conventional digital-to-analog conversion concepts.

The major problem was that the current sources could not be defined as necessary, since the transistors have to operate in their saturation region which could be established for all signals. One requirement would be, that the output voltage only vary between $V_{ss} + V_{ds,sat}$ and $V_{dd} - V_{ds,sat}$. As simulation showed, this problem occurred for both the high and the low side switching transistor and can be seen that the relative slopes do not scale with the presented slopes. Non ideal switching occurs which made it necessary to average the current over time. The problem of not perfect switching is, that the channel is opened and closed slowly in comparison to an ideal switch since the gate of the switching transistor has to be charged which take impact on the driver circuit. A leakage current over the driver circuit is observed which further increase the problem. The different behaviour for the switching process of the separate push-pull stages led to a different set of slopes.

As no complementary transistors were available in III-V technology, a proper driver circuit had to be investigated. Implementation of a known concept [15] for the driver circuit. The dimension of the used components were calibrated with respect to the resulting voltage step at an output capacitance which represent the input stage of a power amplifier. The dimension of the used components was a bottleneck since it limits the signal bandwidth. Small transistor dimensions could synthesize signals with low frequencies and big dimension with high frequencies. Therefore the signal bandwidth was investigated to be roughly 1.5 GHz to 6 GHz.

Different wave forms could be synthesized (sine wave, rectified sine, triangular). With an OSR of four $f_{sampling}$ is eight times f_{signal} which has to fit to the transistors unity gain frequency. For an increase of the OSR the signal quality is better but the power consumption also linearly scale with it. The OSR is limited to the fact that two successive samples have to be distinguished. A sampling interval which is too small can lead to a non detectable voltage step.

Parasitic and loss effects distorted the waveforms. The highest SNR (32.5 dB) found was

for a sine wave at 6 GHz with an amplitude of $\hat{v} = 1.75V$, an DC-offset of $V_{DC} = 13V$ and a phase shift of $\phi = -\pi/8$, see appendix E. The system is stable. The stability check was needed to validate that the circuit did not oscillate. The energy consumption is critical and is rather in the range for base stations than for mobile devices. For an increase in signal quality, the resolution could be increased but the whole circuit would become more complex and the energy consumption would increase. Shifting the baseband to even higher frequencies is possible but the bandwidth stays constant while the power consumption is increased. The designed test circuit is a proof of concept. Nevertheless the simulation results confirmed the feasibility of generating different signals.

In the realisation and layout process many things had to be considered. Important for the design of the input lines were that they are of the same length, due to timing issues, as for the bond wires of the in- and output. The input timing is crucial due to the fact that the switches have to switch synchronous. One of the most important and crucial things was the dissipation of heat. Two concepts were presented to dissipate the heat in the most proper way which were fabricated by CONTAG AG. An improvement for the layout, could be to solder the chips on an electrical insulator while thermal good conductor, as AluminiumNitrid (AlN: 180-200 W/mK -> datasheet).

In a first measurement it was shown that the designed circuit converts a digital signal to an analog one. The measurement follows the expectations of the simulation. Aside from some parasitic effects the proof of the concept was successful.

The design and processing of a MMIC structure containing the Riemann Pump was beyond the scope of this thesis. The calculation of the Riemann Code have to be done with an external signal processor, which has to compute this code in real time. With the ability to change the reference current and the oversampling ratio it is possible to create arbitrary waveforms. In a more enhanced project a MATLAB algorithm would compute this code by minimizing the deviation between a theoretical signal and the synthesized signal.

Bibliography

- [1] F. Rivet, Y. Deval, and B. D. Begueret J.-B., Dallet D., “A Software-Defined Radio based on Sampled Analog Signal Processing Dedicated to Digital Modulations,” in *Research in Microelectronics and Electronics Conference*, 2007, pp. 121 – 124.
- [2] Y. Deval, F. Rivet, Y. Veyrac, N. Regimbal, P. Garrec, R. Montigny, D. Belot, and T. Taris, “Full Software Radio Transceivers,” in *ASIC (ASICON), 2013 IEEE 10th International Conference*, 2013, pp. 1 – 4.
- [3] F. Rivet, Y. Deval, B. J.-B., D. Dallet, P. Cathelin, and D. Belot, “The Experimental Demonstration of a SASP-Based Full Software Radio Receiver,” in *IEEE Journal of Solid-State Circuits*, vol. 45, no. 5, 2010, pp. 979 – 988.
- [4] S. Grossman, “Software-defined radio poses major challenges for hardware and software developers,” *Defense Electronics*, 2005.
- [5] S. Maroldt, “Gallium Nitride Based Transistors for High-Efficiency Microwave Switch-Mode Amplifiers,” Ph.D. dissertation, Albert-Ludwigs Universität Freiburg im Breisgau, June 2010.
- [6] M. W. Chamberlain, “A software defined HF radio,” in *MILCOM 2005 - 2005 IEEE Military Communications Conference*, vol. 4, 2015, pp. 2448 – 2453.
- [7] C. Li, A. Raghunathan, and N. K. Jha, “An architecture for secure software defined radio,” in *Design, Automation & Test in Europe Conference & Exhibition*, 2009, pp. 448 – 453.
- [8] F. Rivet, F. Fadhuile, Y. Deval, and T. Taris, “Wide-Band Rejection of Interfering Signals,” in *IEEE 20th International Conference on Electronics, Circuits, and Systems (ICECS)*, 2013, pp. 767 – 770.
- [9] F. Rivet, Y. Deval, and B. J.-B. D. D. C. P. B. D., “A Disruptive Receiver Architecture Dedicated to Software-defined Radio,” in *IEEE Transactions on Circuits and Systems II: Express Briefs*, ser. 344 - 348, vol. 55, no. 4, 2008.
- [10] D. Y. Rivet F., “A 97mW 0-4GHz 65nm CCMOS Concurrent Receiver,” in *12th IEEE International Conference on Solid-State and Integrated Circuit Technology (ICSICT)*, 2014, pp. 1–3.

- [11] Y. Veyrac, F. Rivet, Y. Deval, D. Dallet, P. Garrec, and R. Montigny, “The Riemann Pump: a Concurrent Transmitter in Gan Technology,” in *21st IEEE International Conference on Electronics and Circuits and Systems (ICECS)*, 2014, pp. 594 – 597.
- [12] Y. Deval, F. Rivet, and Y. Veyrac, “Design by Mathematics of Full Software Radio circuits and systems: methodology and application to 5G standard,” in *EUROPEAN MICROWAVE WEEK*, 2015.
- [13] Y. Veyrac, F. Rivet, Y. Deval, D. Dallet, P. Garrec, and R. Montigny, “A 65 nm CMOS DAC Based on a Differentiating Arbitrary Waveform Generator Architecture for 5G Handset Transmitter,” in *IEEE TRANSACTIONS ON CIRCUITS AND SYSTEMS - II: EXPRESS BRIEFS*, vol. 63, no. 1, 2016, pp. 104 – 108.
- [14] W. Kester, *Taking the Mystery out of the Infamous Formula, " SNR = 6.02N + 1.76dB," and Why You Should Care*, Analog Devices, 2009, mT-001 TUTORIAL.
- [15] Y. Zhang, M. Rodríguez, and D. Maksimović, “100 MHz, 20 V, 90% efficient synchronous buck converter with integrated gate driver,” in *2014 IEEE Energy Conversion Congress and Exposition (ECCE)*, Sept 2014, pp. 3664–3671.
- [16] R. Quay, *Gallium Nitride Electronics*, ser. Springer Series in Materials Science; 96. Springer, Berlin, Heidelberg, New York, 2008, 469 S.
- [17] M. Seelmann-Eggebert, T. Merkle, F. van Raay, R. Quay, and M. Schlechtweg, “A systematic state space approach to large-signal transistor modeling,” *IEEE Transactions on Microwave Theory and Techniques*, vol. 55, no. 2, pp. 195–206, Feb 2007.
- [18] R. Quay, “Script of the Lecture RF- and Microwave Devices and Circuit, IMTEK Freiburg University,” Aug. 2014, version 7.0.
- [19] B. L. Gilmore R., *Practical RF Circuit Design for Modern Wireless Systems*. ARTECH HOUSE, Inc., 2003, vol. 2 Active Circuits and Systems.
- [20] *Keysight Fundamentals of Arbitrary Waveform Generation, A high performance AWG primer, Reference Guide*, 4th ed., Keysight Technologies Deutschland GmbH, Herrenberger Str. 130 71034 Böblingen, Germany, June 2015.
- [21] N. Caka, M. Zabelli, M. Limani, and Q. Kabashi, “Impact of MOSFET parameters on its parasitic capacitances,” in *Proceedings of the 6th WSEAS Int. Conf. on Electronics, Hardware, Wireless and Optical Communications*, February 2007.

- [22] V. Carrubba, S. Maroldt, M. Musser, E. Ture, M. Dammann, F. van Raay, R. Quay, P. Brückner, and O. Ambacher, “High-Efficiency, High-Temperature Continuous Class-E Sub-Waveform Solution AlGaN/GaN Power Amplifier,” in *IEEE Microwave and Wireless Components Letters*, vol. 25, no. 8, 2015, pp. 526 – 528.
- [23] N. Deltimple, L. Leyssenne, E. Kerhervé, Y. Deval, and D. Belot, “Dynamic Biasing Techniques for RF Power Amplifier Linearity and Efficiency Improvement,” in *IEEE International Conference on Integrated Circuit Design and Technology*, 2010, pp. 232 – 235.
- [24] J. Everts, J. Das, V. den Keybus J., M. Germain, and J. Driesen, “GaN-Based Power Transistors for Future Power Electronic Converters,” in *IEEE Benelux Young Researchers Symposium (YRS2010) ,Leuven (Belgium)*, vol. 5, 2010.
- [25] I. S. Ghosh, U. Altmann, O. Kersten, M. Quibeldy, R. Follmann, P. Hildenhaben, M. Rittweger, L. Cabria, E. Cipriani, P. Colantonio, N. Aylon, and A. Chowdhary, “A 250 nm CMOS / LDMOS Pulse-Width Modulator and Driver for space-borne GaN switch mode power amplifiers in P-band,” in *11th European Radar Conference (EuRAD)*, 2014, pp. 356 – 359.
- [26] M. P. van der Heijden and M. Acar, “A radio-frequency reconfigurable CMOS-GaN class-E Chireix power amplifier,” in *IEEE MTT-S International Microwave Symposium (IMS2014)*, 2014, pp. 1 – 4.
- [27] M. P. van der Heijden, M. Acar, and S. Maroldt, “A package-integrated 50W high-efficiency RF CMOS-GaN class-E power amplifier,” in *IEEE MTT-S International Microwave Symposium Digest (IMS)*, 2013, pp. 1 – 3.
- [28] M. P. van der Heijden, M. Acar, J. S. Vromans, and D. A. Calvillo-Cortes, “A 19W high-efficiency wide-band CMOS-GaN class-E Chireix RF outphasing power amplifier,” in *IEEE MTT-S International Microwave Symposium Digest (MTT)*, 2011, pp. 1 – 1.
- [29] Y.-P. Hong, K. Mukai, H. Gheidi, S. Shinjo, and P. M. Asbeck, “High efficiency GaN switching converter IC with bootstrap driver for envelope tracking applications,” in *IEEE Radio Frequency Integrated Circuits Symposium (RFIC)*, 2013.
- [30] C. Jarray, A. Bouabid, and B. Chibani, “Enabling and challenges for 5G Technologies,” in *World Congress on Information Technology and Computer Applications Congress (WCITCA)*, 2015, pp. 1 – 9.

- [31] S. Maroldt, P. Brückner, R. Quay, and O. Ambacher, “A microwave high-power GaN transistor with highly-integrated active digital switch-mode driver circuit,” in *IEEE MTT-S International Microwave Symposium (IMS2014)*, 2014, pp. 1 – 4.
- [32] S. Maroldt, C. Haupt, R. Kiefer, W. Bronner, S. Mueller, W. Benz, R. Quay, and O. Ambacher, “High Efficiency Digital GaN MMIC Power Amplifiers for Future Switch-Mode Based Mobile Communication Systems,” in *Annual IEEE Compound Semiconductor Integrated Circuit Symposium*, 2009, pp. 1 – 4.
- [33] S. Maroldt, R. Quay, C. Haupt, and O. Ambacher, “Broadband GaN-Based Switch-Mode Core MMICs with 20 W Output Power Operating at UHF,” in *IEEE Compound Semiconductor Integrated Circuit Symposium (CSICS)*, 2011, pp. 1 – 4.
- [34] Maroldt, S., R. Quay, C. Haupt, R. Kiefer, D. Wiegner, and O. Ambacher, “Integrated-Schottky-Diode GaN HFETs for High-Efficiency Digital PA MMICs at 2 GHz,” in *40th Microwave Conference (EuMC)*, 2010, pp. 636 – 639.
- [35] R. S. Pengelly, S. M. Wood, J. W. Milligan, S. T. Sheppard, and W. L. Pribble, “A Review of GaN on SiC High Electron-Mobility Power Transistors and MMICs,” in *IEEE Transactions on Microwave Theory and Techniques*, vol. 60, no. 6, 2012, pp. 1764 – 1783.
- [36] D. M. Pozar, *Microwave Engineering*, 4th ed. John Wiley & Sons, Inc., 2012.
- [37] R. Quay and S. Maroldt, “Design and modelling challenges for advanced class-S digital transmitters,” in *Workshop on Integrated Nonlinear Microwave and Millimetre-Wave Circuits (INMMIC)*, 2011, pp. 1 – 4.
- [38] U. Schmid, R. Reber, S. Chartier, W. Grabherr, R. Leberer, and M. Oppermann, “Advances on GaN based switch mode amplifiers for communication applications,” in *41st European Microwave Conference (EuMC)*, 2011, pp. 163 – 166.
- [39] S. Vitanov, V. Palankovski, S. Maroldt, and R. Quay, “Non-linearity of transconductance and source–gate resistance of HEMTs,” in *Proc. European Solid-State Device Research Conf. Fringe Poster Session*.
- [40] A. Wentzel, C. Meliani, and W. Heinrich, “A voltage-mode class-s power amplifier for the 450MHz band,” in *European Microwave Conference (EuMC)*, 2010.
- [41] D. M. Y. Zhang, M. Rodriguez, “High-Frequency Integrated Gate Drivers for Half-Bridge GaN Power Stage,” *Workshop on Control and Modeling for Power Electronics (COMPEL)*, 2015.

- [42] A. Zhang, L. Zhang, Z. Tang, X. Cheng, Y. Wang, K. J. Chen, and M. Chan, “Analytical Modeling of Capacitances for GaN HEMTs, Including Parasitic Components,” in *IEEE Transactions on Electron Devices*, vol. 61, no. 3, 2014, pp. 755 – 761.

Appendix

A. Schematic of the Riemann Pump circuit for simulation

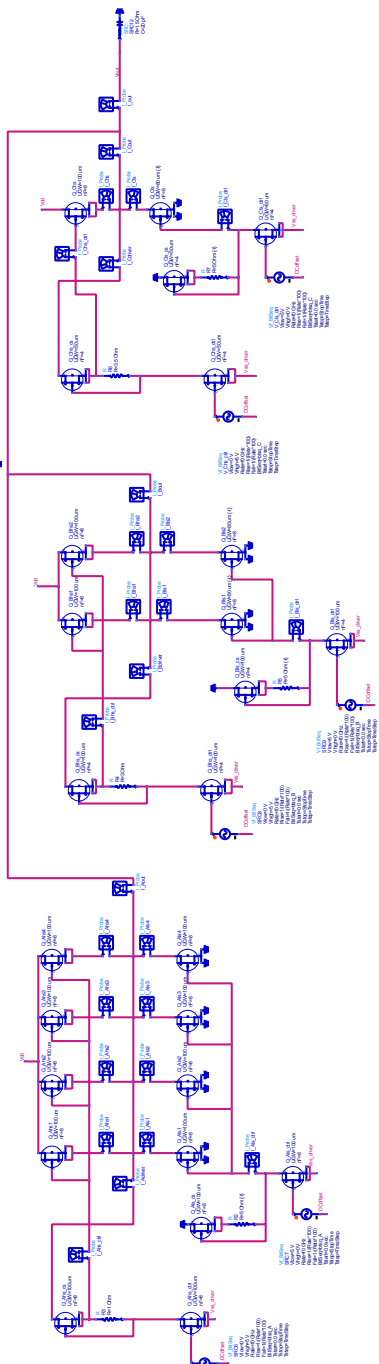


Fig. .1.: Circuit for simulation

B. Schematic of the realized Riemann Pump circuit

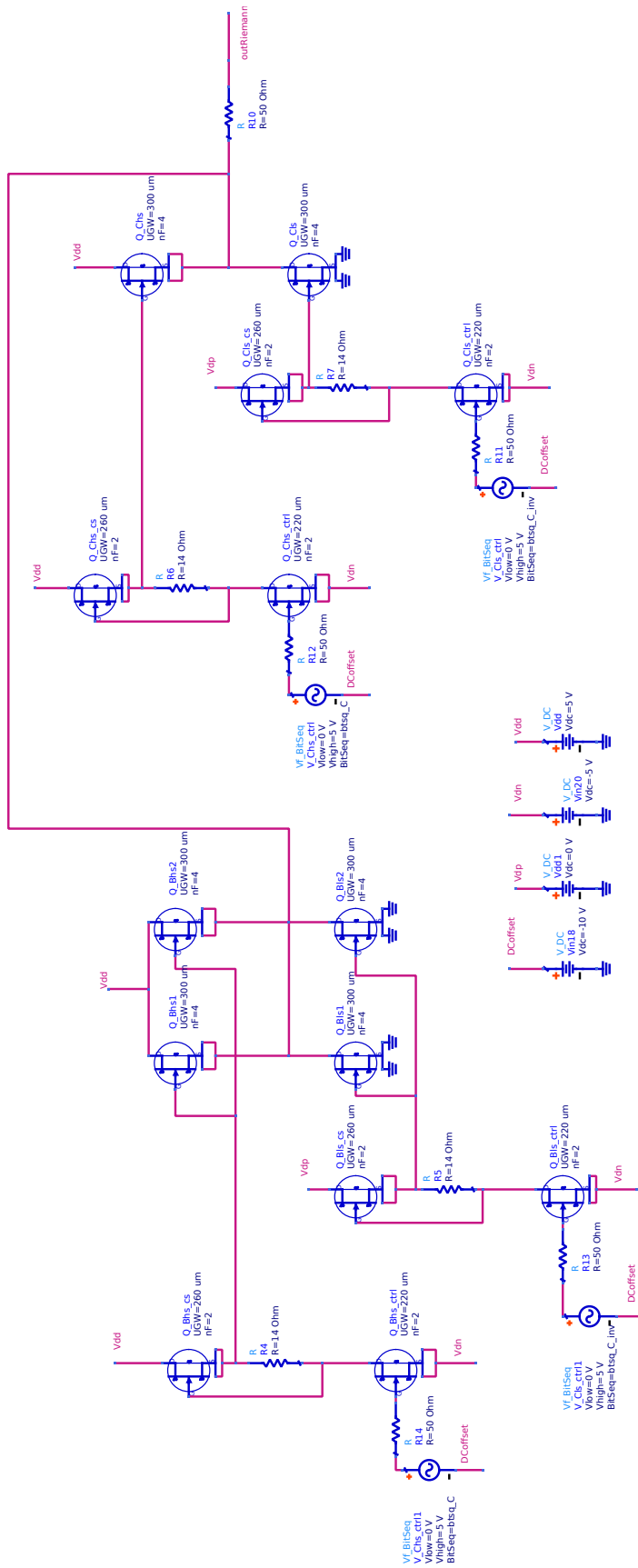


Fig. .2.: Realized test circuit with ADS

C. Photography of the realized Demonstrator version 1

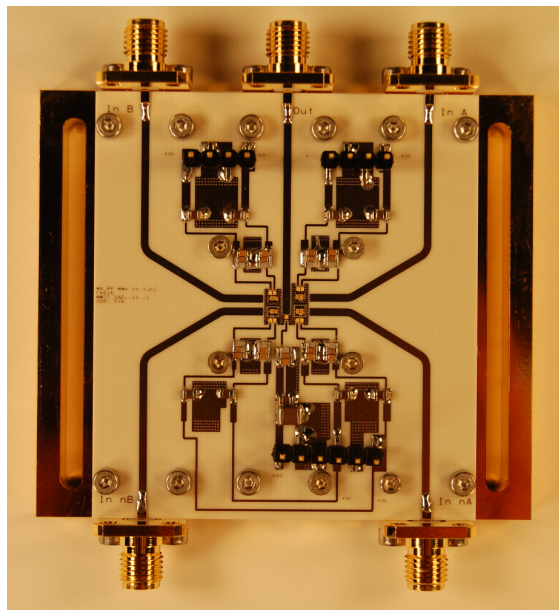


Fig. .3.: Photo demonstrator

D. Photography of the realized Demonstrator version 2

bla bla bla bal bla lbal blalsl

E. SNR Calculation for simulated signals

The calculation of the signal to noise ratio with the corresponding plots is stated here, for the generation of a sine wave with the Riemann Code:

$$000 \ 010 \ 101 \ 111 \ 111 \ 101 \ 010 \ 000. \quad (1)$$

Table .1 states the parameter used for the desired theoretical sine wave.

Table .1.: Calculated SNR and corresponding parameters for the theoretical sine wave

frequency [GHz]	0.5	1	2	3	4	5	6
SNR [dB]	12.7	15	21.1	28.3	27.9	31.9	32.5
amplitude [V]	7.5	7.5	6.5	4.5	3	2	1.75
offset [V]	7.5	7.5	7.5	10	11.5	12.5	13
phase [rad]	$\pi/4$	$\pi/4$	0	$-\pi/16$	$-\pi/16$	$-\pi/8$	$-\pi/8$

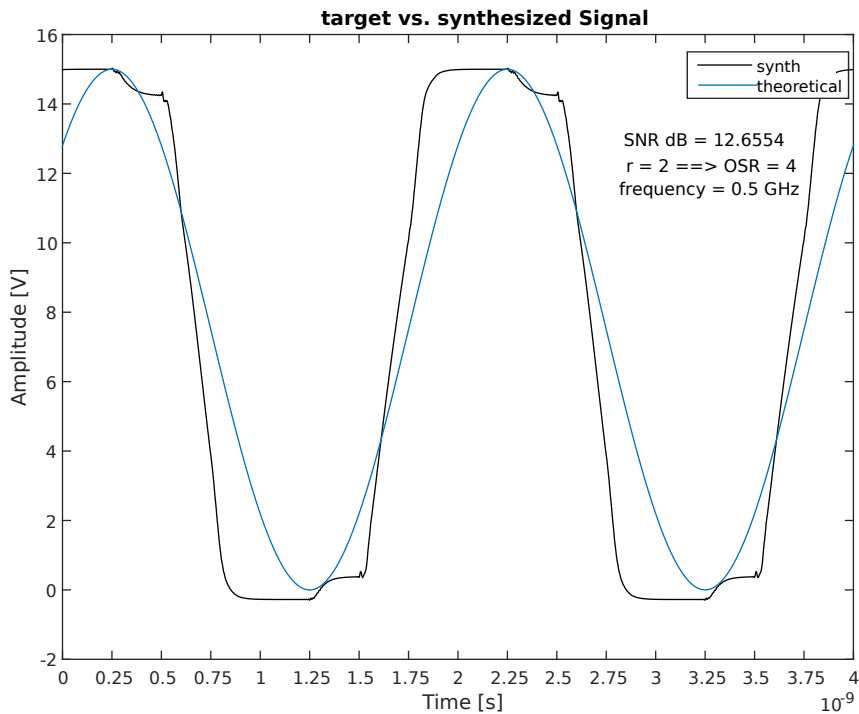


Fig. .4.: calculated SNR[dB]=12.7 sine wave ($f = 0.5$ GHz)

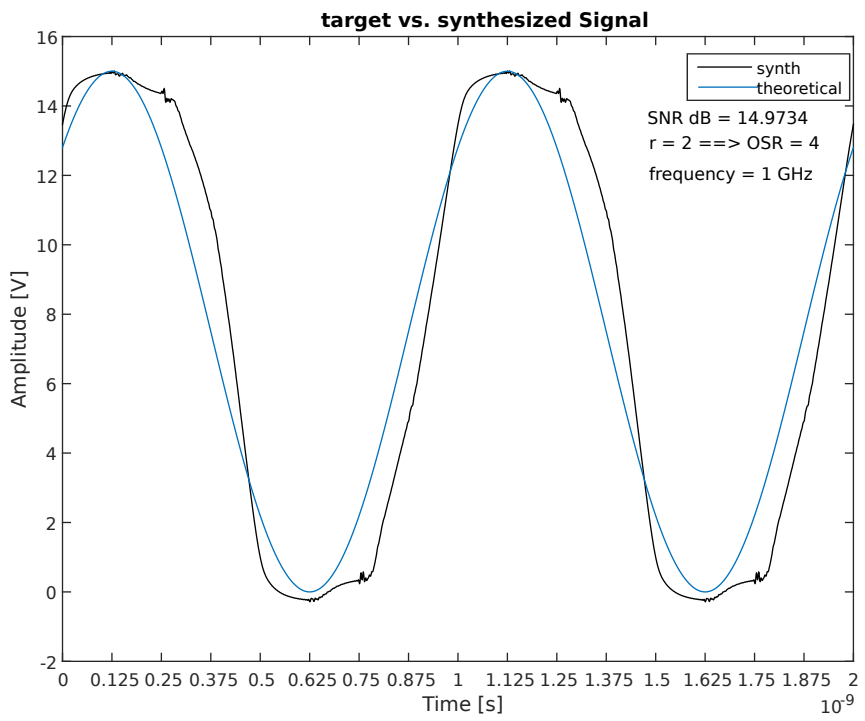


Fig. .5.: calculated SNR[dB]=15 sine wave (f = 1 GHz)

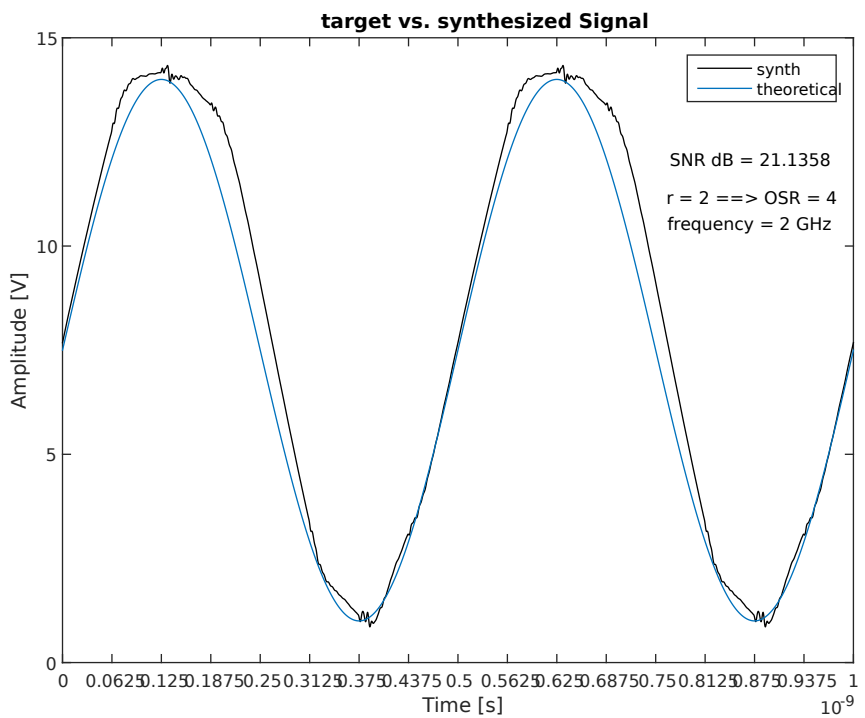


Fig. .6.: calculated SNR[dB]=21.1 sine wave (f = 2 GHz)

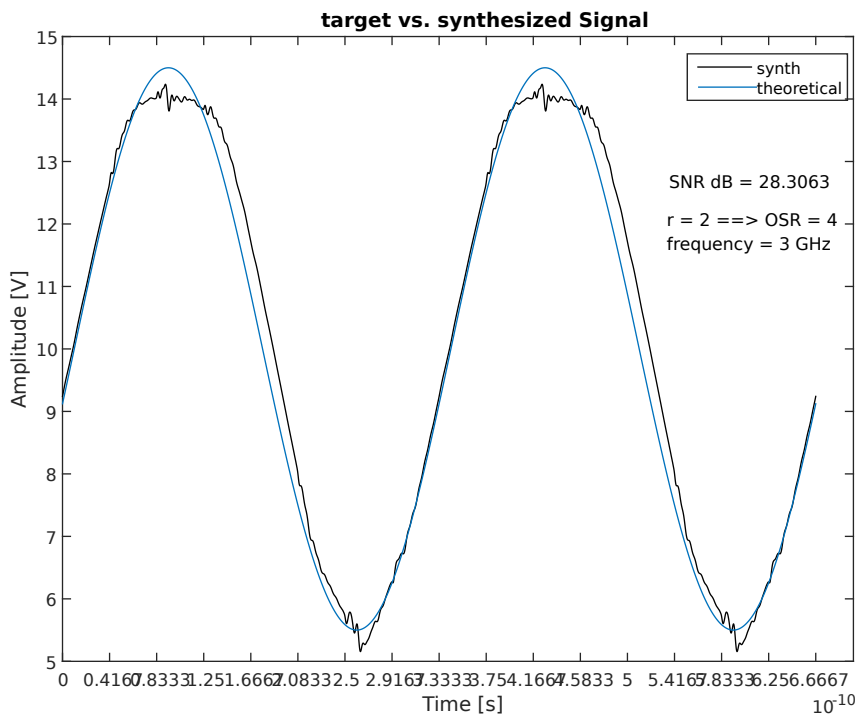


Fig. .7.: calculated SNR[dB]=28.3 sine wave ($f = 3$ GHz)

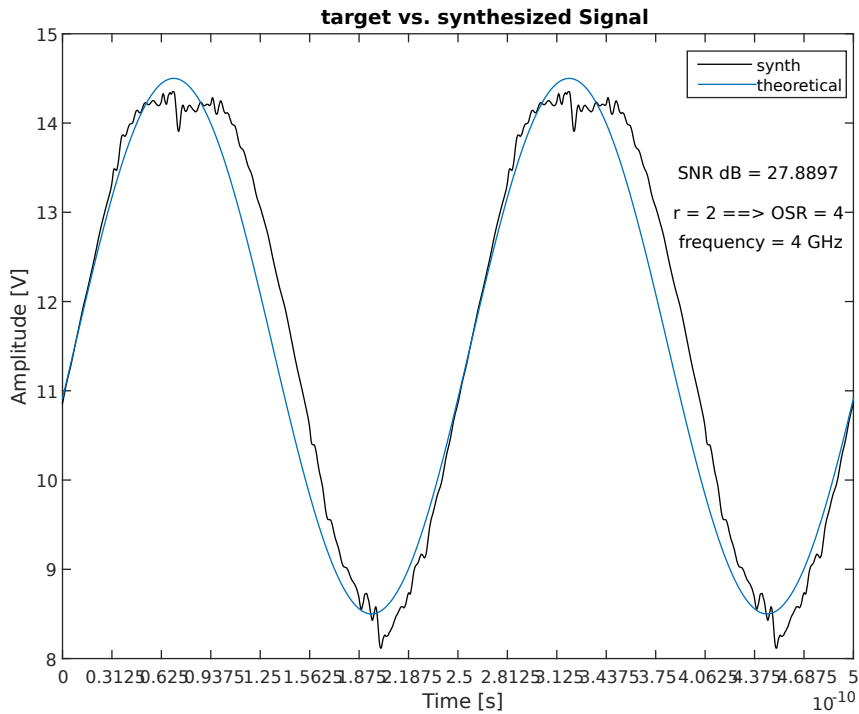


Fig. .8.: calculated SNR[dB]=27.9 sine wave ($f = 4$ GHz)

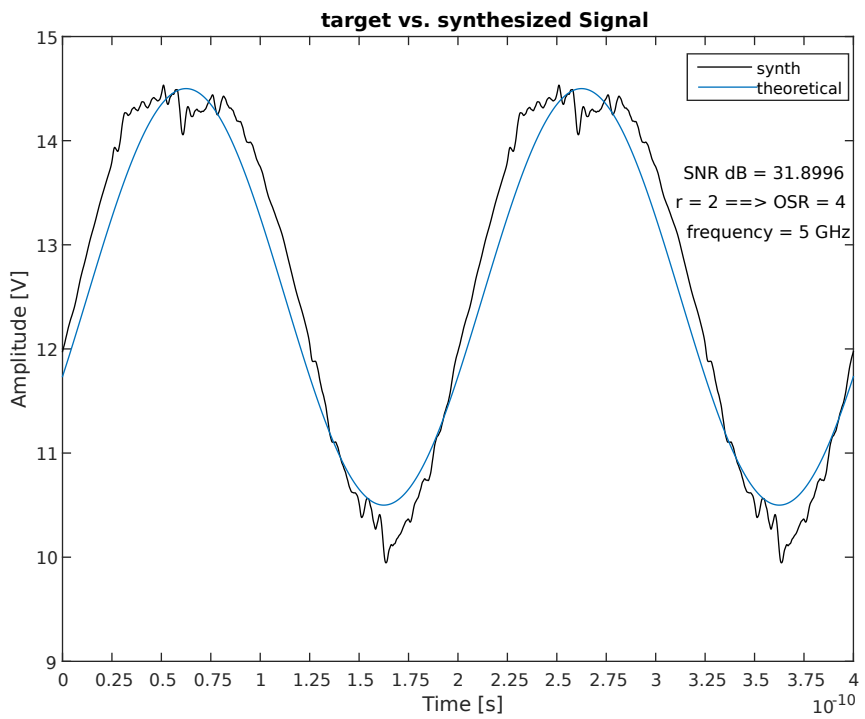


Fig. .9.: calculated SNR[dB]=31.9 sine wave ($f = 5 \text{ GHz}$)

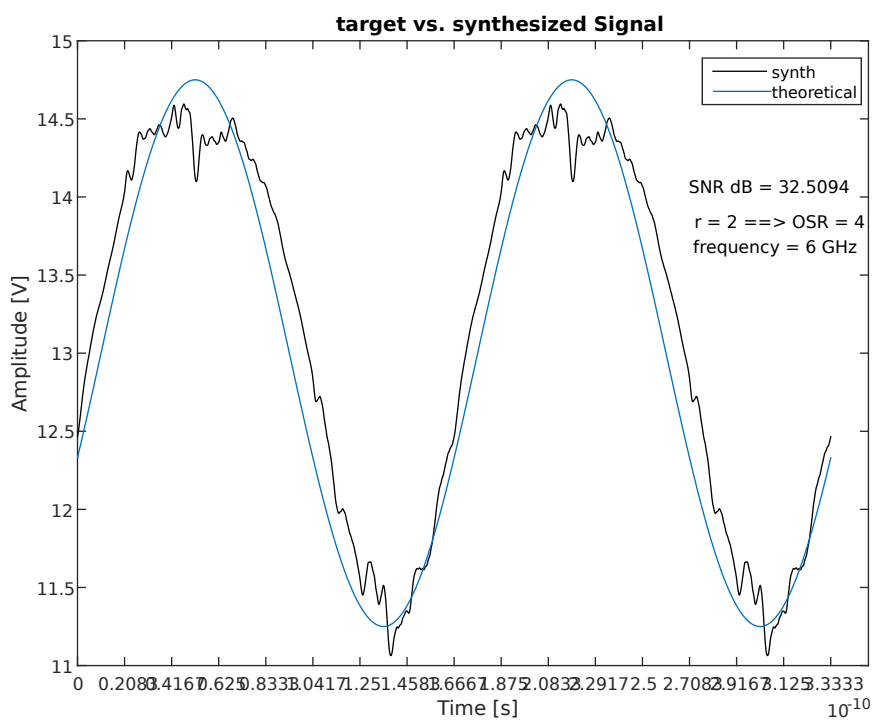


Fig. .10.: calculated SNR[dB]=32.5 sine wave ($f=6 \text{ GHz}$)